

Materials Advances

Accepted Manuscript

This article can be cited before page numbers have been issued, to do this please use: S. M. Chowdhury and S. Akther, *Mater. Adv.*, 2026, DOI: 10.1039/D6MA00156D.



This is an Accepted Manuscript, which has been through the Royal Society of Chemistry peer review process and has been accepted for publication.

Accepted Manuscripts are published online shortly after acceptance, before technical editing, formatting and proof reading. Using this free service, authors can make their results available to the community, in citable form, before we publish the edited article. We will replace this Accepted Manuscript with the edited and formatted Advance Article as soon as it is available.

You can find more information about Accepted Manuscripts in the [Information for Authors](#).

Please note that technical editing may introduce minor changes to the text and/or graphics, which may alter content. The journal's standard [Terms & Conditions](#) and the [Ethical guidelines](#) still apply. In no event shall the Royal Society of Chemistry be held responsible for any errors or omissions in this Accepted Manuscript or any consequences arising from the use of any information it contains.

Spin-Selective Orbital Reconfiguration and Colossal Nonlinear Anisotropy in Defect-Engineered Atomically Thin Quantum Dots

Saraf Mohaimen Chowdhury^a, Salena Akther^{b,c*}

^aDepartment of Electrical and Electronic Engineering, Port City International University, Chattogram 4202, Bangladesh

^bDepartment of Natural Science, Port City International University, Chattogram 4202, Bangladesh

^cDepartment of Mathematics, Chittagong University of Engineering and Technology, Chattogram 4349, Bangladesh

*Correspondence: salenaakther@portcity.edu.bd

Abstract

Spin-texture and wavefunction modification is still a central problem in the attempt to control spin orientation and distribution, effective spin transport, minimized energy dissipation, and improve functionality in spin-based information processing. Here, we studied a specific combination of atomically thin, nonmagnetic, group-13-based post-transition-metal–chalcogenide (PTMC) quantum dots ($M_{10}X_{12}$; $M = \text{Ga, In, Tl}$; $X = \text{S, Se, Te}$) with a single transition-metal (Zr, Mo, Mn) introduced at the central site using density functional theory. It is observed that the spatial distributions of frontier orbitals are not only spin-selective but also site-selective in real-space due to the induced TM– X_3 hybridization, which could allow independent tuning of both spin and spatial characteristics simultaneously. The normalized density overlap can differ by up to 10^{-3} , whereas the normalized signed-amplitude overlap of the corresponding wavefunctions can reach values less than or equal 10^{-4} . The local and effective magnetic moments of M_9TMX_{12} structure can range from $1 \rightarrow 7 \mu_B$ and $1.62 \rightarrow 20.93 \mu_B$, respectively, while the spatial extent of identical-spin orbitals can differ by up to ~ 197 a.u. Moreover, energy-gap of the pristine combination ranges between 0.89–5.02 eV, and it widens upon TM-substitution for E_g^\uparrow (2.6–5.41) while narrowing for E_g^\downarrow (1.62–5.36), which demonstrates that one spin channel can consistently remain energetically more accessible. A clear directional imbalance in the nonlinear optoelectronic response is observed, with the induced polarization switching between in-phase and out-of-phase (phase inversion) based on the field direction. The hyperpolarizability components reach maximum values of up to $\sim 10^6$ (β_{\parallel}) and $\sim 10^9$ ($\gamma_{\parallel}, \gamma_{\perp}$), while the relative distribution between parallel and perpendicular directions remains consistent. Such multifunctional responses resulting from a single-site TM perturbation facilitate fundamental insight into how localized electronic changes simultaneously modulate spin selectivity, orbital anisotropy, and nonlinear polarization as interdependent quantum variables in low-dimensional nanoflakes, which holds promise for the design of multivariable quantum information processing architectures and next-generation nano-spintronic materials.

Keywords: quantum dots; density functional theory; tunable wavefunctions; hyperpolarizabilities; nano-spintronics



1 Introduction

The convergence of low-dimensional quantum materials and spintronics serves as a practical basis to investigate spin-dependent phenomena at the atomic scale. At present, the traditional semiconductor chips heavily rely on bulk materials to achieve charge quantization of carriers for binary logic, rather than spin quantization [1, 2]. Unlike bulk semiconductors with repeating crystal lattices, the two-dimensional (2D) nanoflakes can offer greater efficiency and controllability of electrons due to its finite-scale, surface-dependent, and non-periodic nature [3]. In contrast to the quasi-continuous energy bands exhibited by bulk crystals, 2D nanoflakes referred to as quantum dots (QDs) show discrete energy states which leads to tunable energy gaps [4, 5], sharp absorption/emission [6], edge-dominance [7] and precise carrier localization [8, 9]. Perhaps 2DQDs are currently among the strongest candidates for controlling spin textures, placing them as vital platform for creating novel spintronic and quantum computational devices [10, 11]. Influenced by the atomic sheets of graphene-like materials [12], several classes of other layered materials have been evaluated for different applications. Beyond transition metal dichalcogenides (TMDs), a new set of materials named as post-transition-metal-chalcogenides (PTMCs) have gained enormous interests due to their exceptional property found in polymorph-dependent properties, surface chemistry, optoelectronics, and photovoltaics applications [13–18]. However, previous studies on PTMCs to investigate magnetism include doping induced ferromagnetic (FM) ordering [19], magnetization of nonmagnetic materials [20], vdW magnetism [21], and magnetotransport [22] in bulk or extended 2D structure. Moreover, defect-induced magnetic semiconductors have been studied to understand Curie temperature variation as a function of impurity concentration in PTM-based III–V semiconductors [23], along with strain-tunable magnetic semiconductors for magnetic anisotropy [24] and magnetic proximity effects in non-magnetic–ferromagnetic bilayers [25]. Although much has been achieved, modulation of doping-induced electronic features or redistributions of wavefunction at the single atomic layer scale for much greater controllability has not yet been studied thoroughly, as we require a careful strategy and systematic approach to achieve such subtle modifications.

Previous studies on wavefunction modification in 2D or dot-based system include experimental efforts to understand the electronic structure, charge localization, and optical properties induced with different point defects [26–28], as well as the manipulation of orbital degrees of freedom through inter-dot coupling, dot deformation, or external fields, using microscopy and DFT calculations [29–31]. However, these studies does not answer how the spatial distributions or defect-induced relocalizations of orbitals contribute, which could have built a more constructive understanding of charge localization mechanisms. Present works [32–34] however, address primarily problems and challenges such as electronic wave functions to control optical and electronic properties, orbital quenching from strong crystal field effects, wavefunction overlap in multi-dot arrays, which leads to a loss of well-defined orbitals, and lack of independent control on spin and orbital states. Recently, it has been shown that, unlike conventional TMDs, PTMC-based thin flakes have heavy elements with large atomic masses, which enhance orbital contributions to magnetism and make them a suitable platform to study orbital-dominated and anisotropic magnetic responses [35]. Because their d-orbitals are fully occupied and chemically inert, PTM-based low-dimensional systems tend



to form s-p orbitals interactions when bonded with chalcogens. Due to such characteristics, their ability to respond to point-defect perturbations would likely be more pronounced and the modulation of electronic wavefunctions would be more effective under atomic confinement. Substitutional doping, being one of the earliest and widely used perturbative approaches in semiconductor technology, has long been used to alter the physicochemical properties of materials by introducing localized perturbations in the potential landscape [36]. In Particular, the partially filled d-orbitals of TM atoms can favor manipulation of carrier concentration, Fermi level positioning, defect-induced states, band alignment, and band offsets within the host lattice. In this context, p-d orbital hybridization, by means of substitution of group-13 cations is expected to form localized, symmetry-broken electronic states in real space in confined 2D metal-chalcogenide nanodots. This can minimize orbital quenching and allow greater spatial and spin-orbital control under weak crystal field constraints.

Magnetoelectronic properties are not the only physicochemical characteristics modified by doping, as both linear and nonlinear optical responses are also effectively reconfigured in the nanodots [37, 38]. Previous study reveals how metal substitution in 2D α -In₂Se₃ semiconductors create Janus structures like InGaSe₃ and GaInSe₃ [39] which results in enhancement of nonlinear optical properties, particularly second-harmonic generation (SHG), making them as a promising candidate for advanced photonic devices. Furthermore, recent spectroscopic measurement found that quantifications of third-harmonic generation (THG) is of great importance for layered III-VI compounds as nanoflakes of GaSe and GaTe showed strong third-harmonics peak at the wavelengths of ≈ 520 nm under an excitation wavelength of 1560 nm [40]. Such strong nonlinear optical responses, in both static and dynamic limits, are important for developing applications in electro-optic modulations, optical nano-sensors, and optical communications due to their higher-order susceptibilities [41–43]. Hence, to build a complete description of such interrelated aspects, a constructive theoretical study is essential to account for how a small defect would govern electronic disposition, spatial distribution of spins, and nonlinear polarizations in a confined molecular region.

This work presents a framework to investigate how modification of only a single site in nonmagnetic PTMCs (M₁₀X₁₂; M = Ga, In, Tl and X = S, Se, Te) nanoflakes can lead to the independent control of spatial localization and higher-order hyperpolarizabilities, whose sizes are comparable to the sub-de Broglie length scale. Besides wavefunction relocalization and orbital orthogonality, we found large anisotropic g-factor shifts, high spin-polarization, and spin-selective trap-like localized states, which appear to be a major contributors for having enormous directional linear and nonlinear optoelectronic responses, as observed from the partial density of states (PDOS). The isosurface plots of the highest occupied and lowest unoccupied molecular orbitals (HOMO / LUMO), along with calculation of the electronic spatial extent (ESE), reveal that perturbed wavefunctions can simultaneously exhibit both localization or delocalization characteristics relative to the substituted site, mainly controlled by the unpaired d-electron count ($4d^2$, $4d^5$, $3d^5$). In addition, some QDs exhibit phase-inversion characteristics with a consistent ratio between first- and second- hyperpolarizability relative to the induced polarizations. Overall, these findings show how effectively a nonmagnetic host system can control the intrinsic spin-dependent spatial characteristics over its confined region for possible applications in spintronics, magneto-optical modulation, reconfigurable



quantum logic gates, quantum sensing, magnetic and spin memory technologies.

2 Computational Method

Multifunctional dependencies of the considered nanodots were calculated within DFT approximation and implemented in the Gaussian 16W program [44]. The magneto-electronic and optoelectronic calculations were performed with a range-separated hybrid exchange-correlation functional ω B97X-D [45], and an effective core potential basis set LANL2DZ [46]. To accurately describe the spatial distributions of molecular orbitals in a non-periodic finite size structure, it is important to apply such theories that are able to include long-range exact exchange, reduce self-interaction errors, as well as improve the descriptions of spin-dependent orbital interactions [47, 48]. Both closed-shell and open-shell approach were used to perform geometry optimization on the systems with time-independent self-consistent field (SCF) method to confirm different spin-polarized states. In accordance with Hund's rule, the ground state of the doped-nanoflakes corresponds to a spin-polarized configuration with the highest possible multiplicity, as it minimizes the total energy. All triangular QDs were fully optimized on the potential energy surface until the maximum force converged below 1.5×10^{-5} Hartree/Bohr and the RMS change in the density matrix fell below 1.5×10^{-8} Hartree/Bohr. Spin-orbit coupling effects are captured perturbatively through the orbital-Zeeman and g-tensor contributions. The g-tensors were determined with the Gauge-Including Atomic Orbital (GIAO) method, and linear/nonlinear optoelectronic tensors were calculated with the finite-field method. The detailed computational methods are provided in the *supplementary information*.

3 Results and Discussion

The discussion of magneto-electronic and nonlinear optoelectronic responses are organized into five interconnected parts: (i) core electronic trends, (ii) frontier orbital characteristics, (iii) orbital spatial extent, (iv) magnetic strength and spin-dependent response, and (v) static optical response. In the first subsection, we discuss the systematic, controllable electronic features observed in the considered nanodots. In the following subsection, the rearrangement and redistribution of the molecular orbitals are discussed within a broader scientific context. In the next subsection, we describe the resultant intrinsic characteristics and patterns of the orbital wavefunctions in both pristine and centrally substituted configurations. The discussion is then continued to address the observed magnetic responses and field-induced magnetic characteristics. Finally, our discussion comes to an end by highlighting notable nonlinear components and their hybridization-dependent characteristics across different substituted configurations, followed by a concise summary of a few possible ways to validate these results experimentally.

Before going into the detailed discussion, an overview of the figures are presented briefly. [Figure 1](#) and [Figure 2](#) show the atomic structure of the quantum dots discussed in this work. [Figure 3\(a–c\)](#) describes the projections of the total contributions from each orbital's density of states in the quantum dots. [Figure 4](#) represents the HOMO and LUMO distributions of the pristine configurations, while [Figure 5\(a–i\)](#) depicts



the spin-dependent HOMO-LUMO distributions in the centrally perturbed configurations. Figure 6 shows how the spin-densities are spread across different spatial regions. Finally, Figure 7 compares the directional uniformity preserved in the systems, even after the increment in their respective anisotropic components. The following subsections describe these figures in detail, using a topic-based order that best supports the flow of the discussion rather than a strict numerical order.

3.1 Core Electronic Trends

We begin this analysis by presenting the structural information and addressing the stability of the considered structures. We then describe the overall trends observed in several electronic descriptors, and conclude by discussing how the observed features exhibit clear tunable spin-dependent responses. The structural dimensions and local bonding of the pristine and central-site substituted nanoflakes were quantified using the maximum atomic extent, radius of gyration, and bond lengths. As presented in Table 1, the D_{max} was calculated as the largest distance between any two atoms in the configuration, and the R_g was computed from the root-mean-square distance of all atoms from the center of mass. The corrugation measures how much atoms deviate out-of-plane relative to the nanoflake's planar structure (i.e., buckling), which helps to understand the presence of any local distortions. These descriptors provide a quantitative measure of the overall size and compactness of the finite nanoflake structures. Across all systems, the pristine nanoflakes exhibited planar configurations with zero corrugation and average bond lengths ranging from 2.345 Å ($\text{Ga}_{10}\text{S}_{12}$) to 2.937 Å ($\text{Tl}_{10}\text{Te}_{12}$), while D_{max} values varied from 12.733 Å to 15.586 Å and R_g from 5.021 Å to 6.269 Å. Upon substitution, the nanoflakes maintained planarity, with only minor changes in D_{max} (e.g., 13.110 Å for $\text{Ga}_9\text{ZrS}_{12}$ vs. 12.733 Å for $\text{Ga}_{10}\text{S}_{12}$) and R_g (5.034 Å vs. 5.021 Å). Dopant-neighbor bond lengths were measured for each locally perturbed system, that shows values consistent with local structural relaxation: 2.523–2.558 Å for Zr–S, 2.517–2.527 Å for Mo–Se, 2.750 Å for Mo–Te, and 2.391–2.525 Å for Mn–chalcogen bonds. Overall, these metrics indicate that the substituted nanodots preserve the global size and compactness of their pristine counterparts while accommodating local bond rearrangements around the site of substitution.

In pristine $[\text{Ga}/\text{In}/\text{Tl}] - [\text{S}/\text{Se}/\text{Te}]$ nanoflakes, the 4p, 5p, and 6p from metal atoms primarily constitutes bonding interaction with chalcogen's 3p, 4p, and 5p orbitals, while the filled d -shells remains spectatorial. The binding energies (E_b) have been derived to measure and quantify these interaction strengths with Eq. 1 (see the SI). As presented in Table 2(b), for all the MX systems it is found that E_b increases when larger chalcogen is placed, due to their more diffuse orbitals and effect on charge redistribution. The highest (3.64 eV) E_b is observed for $\text{Ga}_{10}\text{S}_{12}$, while the lowest (2.53 eV) is derived for $\text{Tl}_{10}\text{Te}_{12}$ in pristine dots. It is also observed that after substitution of a single metal atom with a TM (Zr , Mo , Mn) from the central site, the interaction energy increases, as the TM's partially filled d -orbitals can hybridize more frequently with the orbitals of the host elements. The emergent d - p covalent framework strengthens the interatomic bonding which maintains the same chalcogen-dependent energy hierarchy. The smallest increment (0.2 eV) occurs in Mn-substituted $\text{Tl}_9\text{Te}_{12}$, whereas Mo-substituted $\text{Ga}_9\text{Te}_{12}$ exhibits the largest (0.27 eV). Conceptually, the binding energies shift scales with the electronegativity difference between the



TM dopant and chalcogen:

$$\Delta E_b \propto (\chi_{\text{TM}} - \chi_X)^2$$

where χ_{TM} is the Pauling electronegativity of the TMs and χ_X represents the chalcogens. Due to long-range structural relaxation and electronic redistribution induced by the dopant, the replacement of the host atom by single TM causes a local perturbation in both ionic size and electronegativity. Because these TMs have larger atomic radii and different valence p-orbital energies than the pristine metal atom, the local bonding environment around the substitution site undergoes strain and charge reorganization (as per the dipole moments and isosurface plots). This perturbation propagates along the finite quantum dot geometry, which leads to nonlocal relaxation effects that appear as subtle distortions at the edges (Fig. 2). Although such structural distortions does not leads to unstability of the configurations, as confirmed by the formation energies, vibrational analysis, and energetic response under finite temperature perturbations.

After introducing the TM atoms at the central site, the formation energy is computed as,

$$E_{\text{form}} = E(\text{M}_9\text{TMX}_{12}) + E_M - E(\text{M}_{10}\text{X}_{12}) - E_{\text{TM}}, \quad (1)$$

where $E(\text{M}_9\text{TMX}_{12})$ is the total energy of the defected systems, E_M is the total energy of an isolated host metal atom, $E(\text{M}_{10}\text{X}_{12})$ is the total energy of the pristine system, and E_{TM} is the total energy of an isolated TM atom. As depicted in Table 2(b), the derived substitution energies are found to be exothermic nature and the E_{form} range between -4.2 eV to -5.17 eV, i.e., the TM introduction is energetically well favorable. Such energetic favorability is also observed for their corresponding charged states. The corresponding formation energies are provided in Table S1. In addition to deriving the binding and formation energies, the physical stability of the pristine and perturbed configurations were further confirmed via frequency calculations and ab-initio molecular dynamics. The vibrational analysis provides IR spectra, where spectrum analysis shows that all vibrational frequencies are real (positive), with no imaginary (negative) modes, which indicates that the configurations are dynamically stable and does not exhibit time-divergent atomic displacements (SI Fig. S3). The later calculations are performed to examine whether the observed dynamic stability is also maintained under thermal perturbation (SI Fig. S4). The time-evolution of potential energy of all the structure is evaluated over 5 femtoseconds at an instantaneous perturbation temperature of 300 K. The results show a linear relationship between potential energy, with no abrupt large increases or decreases, which confirms the thermal stability of the nanodots at room temperature. These findings demonstrate that the nanodots remain both dynamically and thermally stable over the investigated temperature range. As a result, experimental synthesis of the pristine and substituted configurations appears feasible under conventional laboratory conditions.

As observed from the PDOS analysis in Fig. 3, the low-lying s-p states are shifted and hybridized with the TM d states, and these overlaps are visible around the HOMO and LUMO regions. The orbital overlap increases compared to the pristine's orbital hybridizations, and the increased p-orbital contribution mainly originates from the high-energy p orbitals introduced by the Ga / In / Tl atoms. The energy levels are more densely spaced around energy gap region, particularly for β -channels, which causes the energy gap to be



lower in that channel for most of the configurations. The pristine nanodots adopt closed-shell singlet ground states in SCF calculations, with all electrons paired in occupied orbitals. The derived HOMO-LUMO gap ranges from 0.89 to 5.02 eV, according to Table 2. For Ga-based nanodots, the highest energy gap is shown by Ga₁₀Te₁₂ (3.5 eV) and the gap keeps reducing when chalcogen changes from Te to S. For the In-based QDs, the gap rises when S→Se (by 0.9 eV) but slightly lowered when Se→Te (by 0.2 eV), while for the Tl-based QDs it sharply reduced by 2.17 eV (for S→Se) and then again shifted by 1.55 eV (for Se→Te). Such non-monotonic behavior arises for In- and Tl-based QDs primarily due to their larger orbital energy ($5p^1$, $6p^1$) compared to the smaller orbital of Ga-based MXs ($4p^1$). The larger orbital tends to be more diffusive, and these diffuse orbitals extend further into space, which can increase orbital interaction range. The replacement with TM atoms causes the energy gaps to split into spin-up (E_g^\uparrow) and spin-down (E_g^\downarrow) orbital channels, and almost for all the systems E_g^\downarrow channel is more energetically accessible, as presented in Table 2(b). Also a considerable widening of 4.41 (E_g^\uparrow) and 4.01 (E_g^\downarrow) eV is observed for Ga₉S₁₂ QD upon Zr substitution. However, this shift notably reduces at E_g^\uparrow (by 1.51 eV) and E_g^\downarrow (by 1.46 eV) when the host metal is replaced by Indium, which indicates a host-dependent orbital hybridization for the chosen dopants. The dipole moment analysis supports such preferences, where it quantifies the charge redistribution for such site-selective perturbations, which results from spatial separation or rearrangement of the HOMO and LUMO (Figs. 5a and 5d, discussed later, thereby reducing their overlap and increasing the gap. Table 2 showed that inclusion of Zr heavily alters the charge distributions (nearly three orders of magnitude) in Ga–S framework in contrast to In–S framework (only ~ 0.67 times). Moreover, a reasonable energy gap increment of 3.06 (E_g^\uparrow), 0.8 (E_g^\downarrow), and 1.83 (E_g^\uparrow), -1.88 (E_g^\downarrow) eV is observed for Ga₉Se₁₂ and Ga₉Te₁₂, respectively, upon introducing a $4d^5$ perturbation. In contrast, the corresponding increments for In₉Se₁₂ and In₉Te₁₂ are relatively modest, at approximately 0.43 (E_g^\uparrow), -3.1 (E_g^\downarrow) eV, and 0.9 (E_g^\uparrow), -2.95 (E_g^\downarrow) eV. A lowering in the E_g^\uparrow -channel is found for both Tl₉S₁₂ and Tl₉Te₁₂ by 0.17 and 1.8 eV, while the E_g^\downarrow -channel drops by 3.08 and 0.35 eV. For Tl₉Se₁₂, the E_g^\uparrow increases by 1.81 eV, whereas the E_g^\downarrow decreases by 0.97 eV. Such variations show how local TM defect site can differently affect the spin-resolved electronic structures across various host compositions.

3.2 Frontier Orbital Characteristics

Here, we attempt to analyze the spin-dependent orbital distribution in real space, which is observed to be site-specific according to the isosurface plots. We first briefly compare different spatial configurations, and then perform a mathematical correlation analysis to determine whether such novel distinctions are only visually apparent or physically substantive in origin.

As presented in the isosurface plots of HOMO and LUMO for the pristine (Fig. 4) and substituted (Fig. 5) cases, for the pristine metal-chalcogenide dots, occupied states are localized at the edge sites as a contribution of more effective local bonding environment, in contrast to the unoccupied states, which tend to be more dispersed and pronounced around the center region. This particular arrangement results from the extended nature of conduction states that are less tightly bound at these atomic sites. As a consequence, substitution with an unpaired d-orbital atom at this site increases the overall binding energy



for the d-orbital–induced hybridization, as depicted in Table 2. According to PDOS analysis, it is also observed that due to such site-specific defect, few spin-dependent localized states appeared within and near the HOMO-LUMO region that has very short amplitudes. These states hybridize with the TM's d-orbitals and form localized wavefunctions that are visible as spatially distinct regions in their corresponding isosurfaces. As a result, these localized regions exhibit not only spin-selectivity but also site-selectivity in physical space. Such spatial-duality is predominantly noticeable for [Ga/In]₉ZrS₁₂, [Ga/In]₉MoSe₁₂, α-Ga₉MoTe₁₂, Tl₉MnS₁₂, α-Tl₉MnSe₁₂, and Tl₉MnTe₁₂ nanoflakes: Figs. 5(a, d, b, e, c, g–i). Such presence of asymmetric hybridization also arises from the large local dipolar differences induced by TM substitution, as reported in Table 2. We find that the charge redistributions in the aforementioned nanodots are significantly increased relative to their pristine counterparts, with reported values of 1633, 1380, 5254, 1888 (a.u.) times for selected systems. These outcomes suggest that the coexistence of such varying spin gaps and spatially non-uniform orbitals may allow the nanodots to host multiple energetically distinct electronic states.

To understand whether these molecular dots can represent multiple independent electronic states simultaneously, one way to verify this theoretically is to measure the spatial correlation between same-spin probability densities. The normalised density-density overlap can tell us whether the observed site-selective nature of the spin-dependent electron-density clouds sharing a common or different space. We can compute this pair-density overlap as,

$$D_{\text{HL}} = \int_{\mathbb{R}^3} |\psi_{\text{H}}(\mathbf{r})|^2 |\psi_{\text{L}}(\mathbf{r})|^2 d\mathbf{r} \quad (2)$$

that is normalized by $(\int |\psi_{\text{H}}(\mathbf{r})|^4 d\mathbf{r})^{1/2} (\int |\psi_{\text{L}}(\mathbf{r})|^4 d\mathbf{r})^{1/2}$ in order to remove the dependence on the absolute spatial localization of individual orbitals and to obtain a bounded, dimensionless measure of relative spatial correlation. As presented in Table 3, the normalized density correlation (\tilde{D}_{HL}) tends to approach zero for most of the QDs. The measured \tilde{D}_{HL} approves our intuition that two electron-density that are separated by a finite energy gap appearantly orthogonal (essentially $\leq 10^{-3}$) in terms of their real-space envelopes for most of the dots. Although this correlation measurement of identical spin-densities with $|\psi|^2$ can only capture the positive phase and disregards signed-amplitudes or nodal structures.

This leads us to measure another quantity which can characterizes the real-space interrelation of spatial phases and nodal structures between two same-spin orbitals, and is rotation-invariant. Because two orbitals may occupy the same spatial region (as per the overlapping envelopes) but have opposite signs or nodes locally, and may possible to address selectively or separately (as they correspond to energetically distinct levels). In order to verify this, the spatial overlap between same-spin orbital wavefunctions is evaluated from the reconstructed three-dimensional wavefunction grids $\psi(x, y, z)$, that are derived from the signed real-space orbital amplitudes $\psi(r)$. The overlap integral S quantifies the spatial correlation between HOMO and LUMO orbitals within a spin channel (which is basically the $\langle \psi_{\text{H}} | \psi_{\text{L}} \rangle$), where the normalized overlap S_{norm} accounts for orbital scaling. Within each spin channel, the overlap integral

$$S = \int_{\mathbb{R}^3} \psi_{\text{HOMO}}(\mathbf{r}) \psi_{\text{LUMO}}(\mathbf{r}) d\mathbf{r} \quad (3)$$



is computed on the common cubic grid; and normalization by

$$\sqrt{\langle \psi_{\text{HOMO}} | \psi_{\text{HOMO}} \rangle \langle \psi_{\text{LUMO}} | \psi_{\text{LUMO}} \rangle}$$

yields S_{norm} . A values of $|S_{\text{norm}}| < 10^{-4}$ (that is near zero) would indicate that the two same-spin orbitals are spatially orthogonal. A normalized overlap approaching near zero indicates the same-spin orbitals that are separated by a well-defined energy gap does not result in significant spatial mixing or hybridization in space (i.e., the asymmetry is distinguishable). As depicted in Table 4, for the same-spin orbital pairs the normalized overlap $|S_{\text{norm}}| < 10^{-4}$ which confirms their spatial orthogonality. This behavior is also aligned with the presented isosurface plots, which visually confirm the non-overlapping and site-selective nature of these orbital-shapes depending only on their spin.

Such existence of spin-selective orbital reconfiguration can further be understand if we observe how the atomic spins are spatially populated, as depicted with spin-density plot (Fig. 6). It is observed that due to the presence of nested TM- X_3 hybridization in the host configuration, the distribution of spin-up (α) and spin-down (β) electronic states varies significantly. This implies that the physical occupation of different spin-dependent orbitals in real-space would be vastly different, and as we can see from the isosurface plots that it is entirely selective of the host structure. Such variations of spin-distribution provides a core intuition that if we introduce site-specific defect with a particular dopant (that has unpaired d-electrons) in the nonmagnetic host to form a localized hybridization, it creates a major imbalance of spins, hence is possible to achieve mapping of electronic orbitals in a way that they would distribute asymmetrically and disparately in the real-space. This intuition is consistent with our findings, as not only from spin-density plots, the PDOS analyses exhibits (*discussed earlier*) that the number of different orbital- and atomic electronic states distributed at distinct energy levels due to the presence of Zr- S_3 , Mo-(Se/Te) $_3$, Mn-(S/Se/Te) $_3$ hybridizations. As a consequence, the α -spin and β -spin orbitals occupy different spatial regions while still hybridizing energetically, and exhibit site-selective localizations, for which, the reconfigurations are real, rational, and spin-dependent. The spin-selective orbital reconfiguration observed in these nanodots originates from a combined effect of dopant electronic structure and local hybridization geometry. First, the d-orbital occupancy of the TMs ($3d^5$, $4d^2$, $4d^5$) determines how many spin-polarized states are available to participate in bonding, which governs whether the resulting orbital reconfiguration is strong, weak, or absent. This electronic configuration gives rise to an exchange splitting between spin-up and spin-down components, and the magnitude of such splitting then energetically separates the E_g^\uparrow and E_g^\downarrow channels and enforces spin selectivity at the level of the frontier orbitals. Moreover, the relative overlap between p- and d-orbitals energy of TM and chalcogens controls which orbitals hybridize and within which energy window, which in turn causes different TM- X_3 motifs to exhibit distinct reconfiguration patterns. It is further evident that the local TM- X_3 coordination symmetry lifts the degeneracy among spatial orbitals, and as a result, the hybridized states are shaped into distinct spatial orientations and nodal structures. Together, these factors give rise to a logical, site-selective, and spin-dependent orbital reconfiguration, that are consistently supported by the spin-density distributions, PDOS features, and real-space isosurface plots.



To further support the real-space orbital and spin-density analyses, we performed Mulliken population analysis for all pristine and centrally perturbed nanodots (*Tables S4–S12*) along with their representative charged state (*Tables S13–S21*). It is observed that the resulting charge and spin populations are consistent with the site-selective and spin-dependent electronic reconfigurations identified from the orbital isosurfaces and overlap analyses. Because Mulliken populations projects the spin-resolved density matrix on to atom-centered basis functions, the observed atom-resolved spin moments represent the total integrated consequence of the spin-selective orbital reconfigurations, that are visually observed in real-space. In the subsequent analysis, we discuss that, apart from the orthogonality of spin-dependent energy states, same spin orbitals also encompass distinct spatial radius, that would provide a more constructive understanding of their spatially independent nature. Collectively, these results imply that most of the nanodot demonstrates quasi-independent like electronic states within their same spin channel, which could inform future experimental efforts.

3.3 Orbital Spatial Extent

The calculation of electronic spatial extent (ESE) provides an outlook into the spatial characteristics of orthogonal wavefunctions that quantifies how each orbital's electron density is distributed in space. It is the expectation value of the squared radial distance $\langle r^2 \rangle$, that was derived from the orbital density as

$$\langle r^2 \rangle = \frac{\sum \psi^*(\mathbf{r})r^2\psi(\mathbf{r})\Delta V}{\sum \psi^*(\mathbf{r})\psi(\mathbf{r})\Delta V}, \quad (4)$$

where ΔV is the voxel volume and the summation over all voxels approximates the integral over space. The continuous integral is then discretized on the 3D cube grid by multiplying each voxel's contribution by its volume and summing over all voxels, which were normalized by the total orbital density to account for non-normalized wavefunctions.

In case of different energy orders with same spins, the quadrupole moment analysis can give a more constructive outlook (see Supporting Information, Table S2), as it quantifies the degree of spatial asymmetry and directional electron density distortion across the molecular framework, and indicates a more spatial polarization and anisotropy in the substituted configurations. As per [Table 4](#), for the same energy order with different spins, we can see that the Zr-S₃ interaction within the host of Ga₉S₁₂ QD, ESE shifts about +155.6 and +91.5 a.u. for the spin-up and spin-down orbitals, respectively. However for the same hybridization, In₉S₁₂ shows an identical distribution of E_g^\uparrow electrons and a reduction of 39 a.u. for E_g^\downarrow . Moreover, configuration like α -Ga₉MoS₁₂, α/β -In₉ZrS₁₂, α -Tl₉MnS₁₂, and α -Tl₉MnSe₁₂ has a comparatively large spatial difference of 158.4, 158.1, 197.37, 93.3, 95 (a.u.), respectively, which tells us that alongside their orthogonal behavior the expansion in real-space deviate such that each of the orbitals can possibly be realized as quasi-independent states (in real space).

For the rest of the dots, the ESE shifts positively and the [Table S3](#) (in the SI) verifies whether the spatial distribution of both spins within the same energy window is identical. We find that the occupied orbitals of



$\text{Ga}_9\text{MoSe}_{12}$, $\text{In}_9\text{ZrS}_{12}$, $\text{Tl}_9\text{MnS}_{12}$, and $\text{Tl}_9\text{MnTe}_{12}$ are non-orthogonal in nature and normalized as

$$\langle \psi_i | \psi_i \rangle = \int \psi_i^*(\mathbf{r}) \psi_i(\mathbf{r}) d\mathbf{r} = 1 \quad (5)$$

Despite such similar distributions, the ESE changes significantly for the virtual orbitals of both spins. This reduction or increment can be understandable if we again observe the spatial dispersion of spin-differential frontier orbitals (as per Fig. 5). For example, in case of the $\text{Ga}_9\text{MoSe}_{12}$ nanodots, we see that HOMOs are distributed along the same spatial location, simultaneously for both channels, but as the dipole moments increased by 1630 times from pristine, the spatial extent of electrons meant to be increased by some amount (+155 au at LUMO in this case). But this explanation may seem contradictory at first look if we observe the $\text{In}_9\text{ZrS}_{12}$, because ESE shifted negatively despite its dipole moment remains same compared to pristine. The main reason this result is not counterintuitive as the local electronic stabilization (dopant-induced potential wells that preferentially localize electrons in certain regions) has more effect on orbital localization than the global dipole variation. Moreover, though $\text{Ga}_9\text{MoSe}_{12}$, $\text{In}_9\text{ZrS}_{12}$, $\text{Tl}_9\text{MnS}_{12}$, and $\text{Tl}_9\text{MnTe}_{12}$ exhibit a clear homogeneity in spatial localization of α -HOMO states localized below the orbital energy gap upon substitution Figs. 5(b, d, g, i), they confirmed higher spin-states like quintet, sextet, and septet. Notably, distinct spin-dependent energy gaps are still present despite this spatial homogeneity. The energy gap difference between alpha and beta channels are 2.26, 0.05, 2.91, and 1.45 (eV), respectively, as reported in Table 2.

Such coexistence of a small but finite density overlap with a vanishing signed wavefunction overlap, as well as distinct spatial extent, shows that these states remain functionally decoupled due to site- and node-selective separation, rather than only phase cancellation within the same region. Moreover, though PDOS depicts the presence of energetic hybridization between dopant and host orbitals, the overlap results show that these states remain spatially distinct and occupies different sites and spatial radii. This spatial separation limits real-space coexistence despite energy-space mixing, which in turn allows the spin-dependent orbitals to behave as distinguishable spatial channels. Such real-space localization suggests that selective excitation or manipulation of site- and spin-specific states could be feasible, which holds promise for memory or logic functionalities at such nanoscale limits. Taken together, the observed anisotropic spatial distribution of orbitals allows us to control each of the parameters independently and suggests that such spin-dependent, site-specific confinement provokes differential localization of orbital polarization, which in-turn gives selective modulation and spatial architecture of frontier orbitals and spin channels.

3.4 Magnetic Strength and Spin-Dependent Response

In this subsection, the goal of the discussion is to structure a constructive analysis on the observed magnetic response, and how the intrinsic as well as the field-induced magnetic behavior recharacterizes spin-dependent interactions in the system. The spin multiplicity (M) is obtained by performing the ground state geometry optimization for different spin-polarized states (quartet, septet, octet etc.), and the one with



the lowest total energy is defined as the magnetic state of that structure. For all configurations studied, we explicitly tested multiple spin multiplicities. We considered states with up to 16 unpaired electrons. In every case, the total energy shows that the highest-spin state is the most stable. This ensures that the identified ground state indeed corresponds to the highest-spin configuration. In all cases, the computed total energies confirmed that the highest-spin state is the most stable, that validates our assumption. The net magnetic moments μ_{net} are derived from the Mulliken spin analysis which represents the sum of all Mulliken spins induced in the system. As depicted, the TM-dopant carries the maximum-site-moment and its magnitude depends on the host elements. As we can see from the SI Tables S4–S12, The Zr-S₃ interactions in Ga₉S₁₂ produces maximum local moment of 1.935 μ_B , and when the host framework constitutes In₉S₁₂ it shows 1.048 μ_B . But for the Mn-S₃ interactions in Tl₉S₁₂ the source magnetic moment can reach up to 4.742 μ_B . It is because when the orbitals are more spatially extended, the spatial overlap with dopant d-orbitals becomes more frequent and higher, which in turn leads to a more hybridization per site. Such observation is similar for the other nested hybridizations, as we can see Mn-Se₃ and Mn-Te₃ tends to produce comparatively higher or equivalent local moments compared to the Mo-Se₃ and Mo-Te₃ interactions with the host.

The magnetic responses of the nanodots when interacting with an external magnetic field are presented in Table 2(c). As presented, the significant shifts in directional g-tensors which increases the effective g-factor are the direct consequences of high spin-orbit coupling (SOC) effect in the nanoflakes. It is because the combined orbital's contribution from transition-metal and heavy-metals to magnetism is much higher and dominating over the spin's contributions. In response to the interaction with a magnetic field, the QDs exhibits an effective magnetic moments which can be quantify as, $\mu_{eff} = g_{eff}\sqrt{S(S+1)}\mu_B$. The g_{eff} is derived from the g-shifts of each principal axis and calculated as their averaged value, where μ_{eff} increases along with the increase in g_{eff} . The computed g-tensors include contributions from orbital-Zeeman and perturbative spin-orbit terms (g_{OZ}/SOC), and the observed anisotropic g-factor shifts primarily arise from orbital-Zeeman contributions, where SOC provides a quantitative corrections. Deviations from the free-electron g-factor indicate enhanced orbital participation and anisotropic magnetic response induced by the dopants. The mean g-factor of the free electron is a key descriptor to understand the spin behavior, where $g_e \sim 2.002$ and any deviation from this value indicates modifications of SOC and exchange interaction in the molecular electronic configurations due to central defects. The deviation of g-factor along the principle is derived with GIAO formalism that are presented details in the methodology section of SI. As we can see, when the effective g-factor increases, the μ_{eff} exhibits higher response, which reflects its ability to enhance orbital-induced magnetism due to the strong presence of SOC. The field-induced magnetic moments due to such effect shows a very strong magnetic moments, as the derived μ_{eff} range between 1.62 μ_B to as much as 20.93 μ_B . This kind of large magnetic response suggests multifunctional magnetic behaviors of these nanoflakes, which shows simultaneous presence of spin-selective orbital distribution is real-space and field-controllable magnetic moments.

The PDOS for all the considered quantum dots is shown in Figs. 3a to 3c, which depict the specific orbitals contributions involved in host-TM hybridization. For the pristine Gallium- and Indium-based MX dots it is observed that metals s, p and chalcogen p orbitals dominate primarily because the d-orbitals remain



stable (appear at very low energies) and do not participate in bonding, staying inactive near or around the energy gap region. Compared to the Thallium-based QDs, some electrons from d-orbitals actively participate in its pristine form in the PDOS, because of its relativistic effects (particularly scalar relativistic contraction of the 6s orbital) and expansion of the 5d shell which raise the energy of the 5d states and enhance their spatial extension. As a result, Tl's 5d orbitals can hybridize appreciably with neighboring p orbitals (from chalcogen atoms and the host configuration), and shows a detectable d-character near the HOMO-LUMO region of the electronic spectrum. A tiny contribution comes up from Zr's 4d² orbitals in the Ga₉S₁₂ and In₉S₁₂ nanodots upon single Zr substitution Fig. 3a, showing a marginal overlaps with the host orbitals. It is worth noting that this limited interaction still contributes to the spin-polarization observed in the quartet (M=4) and doublet (M=2) magnetic states (spin-density isosurface of Figure 6a, 6d), particularly for In₉S₁₂ system, where the spin density are closely confined at the substituted site. In contrast to the Tl₉S₁₂ QDs, Mn substitution results in more noticeable orbital overlap due to its higher number of unpaired d-electrons (3d⁵), and in both spin channels this interaction is visible along the HOMO-LUMO (3c) region. Despite the lower availability of electronic states, the interactions are effective enough to produce high septet polarization, and the resultant magnetic moments show a broad spatial distribution from the center to at an in-plane edge site adjacent to the substituted site (Figure 6g).

Following Mo-induced perturbation in Ga₉Se₁₂, Ga₉Te₁₂, In₉Se₁₂, and In₉Te₁₂ nanoflakes, the orbital interactions lead to much higher spin-polarized states. The presence of 4d⁵ orbitals, which hybridize in the midgap region of Ga₉Se₁₂ (3a), results in asymmetric spin localization around the dopant and at an edge site Figure 6b, similar to what is observed for Ga₉S₁₂ and Tl₉S₁₂ nanoflakes. This sort of spatial separation of spin densities at a peripheral site on the same plane as the dopant is evident in Tl₉Se₁₂ (6h) and Tl₉Te₁₂ (6i) QDs, where d-orbital-induced hybridization via Mn substitution are noticeably stronger and denser (3c).

But a more widespread delocalization of magnetic moment, that extend from the central to peripheral edge sites across the plane, is observed for Ga₉Te₁₂ (6c), In₉Se₁₂ (6e), and In₉Te₁₂ (6f) nanoflakes. The nested Mo-(Se, Te)₃ interactions shifts the low-lying valence states upward in energy through 4d⁵ orbital overlap (3a, 3b), and consequently, the magnetic configuration corresponds to the octet state, which is the highest among the group (Table 2). It is understandable from our PDOS analysis that when the number of overlapping states from hybridized orbitals increases near or above the energy gap, exchange interactions become more strong, which in turn leads to the emergence of site-specific spin textures and higher spin polarization in the system. To provide a more detailed outlook on atomic contributions, the element-projected PDOS is presented in the Supporting Information (Figs. S1).

3.5 Static Optical Response

The anisotropy in $\alpha(0; 0, 0)$, $\beta(0; 0, 0)$, and $\gamma(0; 0, 0)$ has been studied in-reponse to the TM-defect in order to characterize the nature of the material and to understand whether the observed anisotropic magneto-electronic response also present when interacting with a constant electric field, at such confined geometry. The ground-state electron cloud response increases when chalcogen changes from S to Se, Te,



as measured by the average linear polarizability (α_{iso}) and directional polarizability (α_{aniso}) for pristine QDs. The relative ratio between anisotropic and isotropic responses (R_A) provides a quantitative measure of the directional dependency in these nanoflakes. The isotropic and anisotropic responses ranges from $\sim 0.6 \times 10^3$ to $\sim 0.15 \times 10^4$ for the pristine configurations, with values on the order of $\sim 10^4$ observed when the MX dots are bonded with Te, as depicted in Table 5. This behavior is a direct consequence of shifted dipole moments that increases when either the metal or chalcogen atom varies to higher atomic radius. Compare to the substituted configurations, the anisotropic response shows a marginal increase for $\text{Ga}_9\text{MoTe}_{12}$, $\text{In}_9\text{MoSe}_{12}$, $\text{In}_9\text{MoTe}_{12}$, $\text{Tl}_9\text{MnS}_{12}$, $\text{Tl}_9\text{MnTe}_{12}$, but significantly dominates for $\text{Tl}_9\text{MnSe}_{12}$, reaching up to 0.22×10^4 scale.

This large increment due to Mn–Se₃ can be rationalized upon inspection of the corresponding isosurface plots of the HOMO Figs. 5(c, e, f, g, i). They show a highly asymmetric localization of wavefunctions and diffuse orbitals, where the spin-up orbitals are primarily confined to one edge site, while the spin-down orbitals are distributed along a different peripheral site in the opposite direction (yet along the same axis). Such directional separation from the overlap of $6p^1-3d^5-4p^4$ intensifies charge polarization along one axis, which in turn amplifies the anisotropic response of this quantum dot.

More interestingly, the first-hyperpolarizability tensor components (β_{\parallel} , β_{\perp}) exhibits phase (direction of the induced polarization) inversion between the applied electric field and the induced polarization. As shown in Table 4, this phase inversion becomes switchable to in-phase polarization through Zr- and Mo- substitution in pristine $\text{Ga}_{10}\text{S}_{12}$, $\text{In}_{10}\text{Se}_{12}$, $\text{In}_{10}\text{Te}_{12}$, while Mn-substitution in $\text{Tl}_{10}\text{Se}_{12}$ induces an out-of-phase polarization relative to its pristine counterpart. The in-phase polarization increased by roughly $\sim 10^2$ to $\sim 10^4$ times of magnitude, while the out-of-phase response reached up to $\sim 10^3$ times of magnitude in their corresponding β_{\parallel} components. Alongside this, the $\text{Ga}_9\text{MoTe}_{12}$ nanodot exhibits the highest increase, rises approximately six orders of magnitude, and the largest variation between the parallel and perpendicular components is observed for $\text{In}_9\text{ZrS}_{12}$ (R_B reach about 3.06).

In addition, a similar phase reversion in second-hyperpolarizability tensor components (γ_{\parallel} , γ_{\perp}) are also observed for the $\text{Tl}_9\text{MnSe}_{12}$ nanodot, where the intensity reaches approximately 10^9 and 10^8 along the field direction and perpendicular to it, respectively. As reported in Table 5, the third-order nonlinear response is the strongest among all considered QDs, which suggests that such confined geometry, zigzag edge-bonding, and local perturbations give rise to long-range, non-saturating, and significant static nonlinearity in these sub-de Broglie length regimes. The highest anisotropy ratio (R_{Γ}) is observed for the $\text{Ga}_{10}\text{S}_{12}$ nanoflake (~ 3.1), which indicate its wavefunction delocalization Figure 4(a, b) is much more pronounced along the direction of the interacting field. The directional uniformity preserved in the systems, in accordance with such amplified intensities, can be more easily understand from Figure 7.

The predicted spin- and site-selective orbital reconfigurations could be experimentally validated in several ways [49–52]. Spin-polarized scanning tunneling microscopy (SP-STM) can directly visualize the real-space spin densities and reveal the spatial separation between E_g^{\uparrow} and E_g^{\downarrow} orbitals. Another method could be X-ray magnetic circular dichroism (XMCD), which can probe the spin-dependent contributions of the transition-metal dopants and confirm magnetic anisotropy. Moreover, spin-resolved photoemission



spectroscopy (Spin-PES) can measure the energy-level separation between spin-up and spin-down orbitals, which may directly validate the predicted exchange splitting. In addition to this, STM or scanning tunneling spectroscopy (STS) can map the local density of states to confirm site-specific localization of frontier orbitals. X-ray absorption spectroscopy (XAS) or electron energy-loss spectroscopy (EELS) can also probe the symmetry and spatial distribution of unoccupied orbitals. The effective g-factor enhancement due to SOC effect can be confirmed via electron spin resonance (ESR) experiments under applied magnetic fields. Furthermore, linear polarizability and first/second-hyperpolarizabilities can be measured using techniques like electric-field-induced second-harmonic generation (EFISHG), optical absorption spectroscopy, or hyper-Rayleigh scattering (HRS) measurements, which provide information on charge distribution and anisotropy in orbital delocalization.

4 Conclusion

Using DFT, the spatial regulation of spin-dependent frontier orbitals and anisotropy in hyper(polarizabilities) of group-13 based one-atom-thick zigzag-edged PTMC quantum dots is investigated. A metal atom from the host system was substituted with a single TM atom, which forms a nested TM- X_3 region, and a systematic computational approach was used to determine how such confined interactions within a closed-shell structure modifies morphology of electronic orbitals, thus their spatial distributions, spin decoration, and optoelectronic response. Spin-dependent spatial expansion and contraction of wavefunctions were observed, along with edge-centric and spin-down dominated magnetic density and the dominance of longitudinal or transverse hyperpolarizabilities. This study establishes that point-defect-like perturbations in molecular dots can introduce quasi-independent electronic states in real space and induce phase inversion of polarization, which enables control over diverse multifunctional properties important for multivariable quantum information processing technologies.

The edge atoms of the QDs were modeled in their under-coordinated form (without applying explicit passivation) to isolate the intrinsic effects of internal substitutional defects, while TM dopants were placed at a central interior site to ensure a controlled coordination environment. Future work could explore the effects of alternative defect configurations or host stoichiometry, which may include different TM incorporation sites, vacancies, and edge substitutions with appropriate chemical passivation, to establish broader structure-property trends in QDs. Such studies would extend insights into how defect configurations influence the electronic and optical behavior of quantum dots.

Supporting Information

The *Supporting Information* provides additional details and data to complement the main text, including computational methods, structural parameters, formation energies of charged states, charge distribution analyses, spin and orbital projections, total density of states, atomic charges and spin populations, vibrational responses, finite-temperature energy landscapes, and full atomic coordinates of the studied quantum dots.



Data Availability

The data supporting the findings of this study are available from the authors upon reasonable request.

Conflicts of Interest

The authors declare that they have no known competing financial or personal interests that could have appeared to influence the work reported in this paper.

Funding

The authors declare that this research was conducted without any specific financial support from public, commercial, or not-for-profit funding agencies.

References

- [1] Dieny B, Prejbeanu IL, Garello K, Gambardella P, Freitas P, Lehdorff R, Raberg W, Ebels U, Demokritov SO, Akerman J, Deac A, Pirro P, Adelman C, Anane A, Chumak AV, Hirohata A, Mangin S, Valenzuela SO, Onbaşlı MC, D'Aquino M, Prenat G, Finocchio G, Lopez-Diaz L, Chantrell R, Chubykalo-Fesenko O, Bortolotti P. Opportunities and challenges for spintronics in the microelectronics industry. *Nat Electron*. 2020;3:446–459. <https://doi.org/10.1038/s41928-020-0461-5>
- [2] Zwerver AMJ, Krähenmann T, Watson TF, Lampert L, George HC, Pillarisetty R, Bojarski SA, Amin P, Amitonov SV, Boter JM, Caudillo R, Correas-Serrano D, Dehollain JP, Droulers G, Henry EM, Kotlyar R, Lodari M, Lüthi F, Michalak DJ, Mueller BK, Neyens S, Roberts J, Samkharadze N, Zheng G, Zietz OK, Scappucci G, Veldhorst MK, Vandersypen LMK, Clarke JS. Qubits made by advanced semiconductor manufacturing. *Nat Electron*. 2022;5:184–190. <https://doi.org/10.1038/s41928-022-00727-9>
- [3] Gu X, Guo L, Qin Y, Yang T, Meng K, Hu S, Sun X. Challenges and prospects of molecular spintronics. *Precision Chemistry*. 2023;2:1–13. <https://doi.org/10.1021/prechem.3c00071>
- [4] Zhuo Z, Wu X, Yang J. Two-dimensional phosphorus porous polymorphs with tunable band gaps. *J Am Chem Soc*. 2016;138:7091–7098. <https://doi.org/10.1021/jacs.6b02964>
- [5] Ramasubramaniam A, Naveh D, Towe E. Tunable band gaps in bilayer graphene–BN heterostructures. *Nano Lett*. 2011;11:1070–1075. <https://doi.org/10.1021/nl1039499>
- [6] Mi Y, Zhang Z, Zhao L, Zhang S, Chen J, Ji Q, Shi J, Zhou X, Wang R, Shi Gespräch J, Du W, Wu Z, Qiu X, Zhang Q, Zhang Y, Liu X. Tuning excitonic properties of monolayer MoS₂ with microsphere cavity by high-throughput chemical vapor deposition method. *Small*. 2017;13:1701694. <https://doi.org/10.1002/sml.201701694>



- [7] Abdelsalam H, Zhang QF. Properties and applications of quantum dots derived from two-dimensional materials. *Adv Phys X*. 2022;7:2048966. <https://doi.org/10.1080/23746149.2022.2048966>
- [8] Golovynskiy S, Bosi M, Seravalli L, Li B. MoS₂ two-dimensional quantum dots with weak lateral quantum confinement: intense exciton and trion photoluminescence. *Surfaces Interfaces*. 2021;23:100909. <https://doi.org/10.1016/j.surfin.2020.100909>
- [9] Whitham K, Yang J, Savitzky BH, Kourkoutis LF, Wise F, Hanrath T. Charge transport and localization in atomically coherent quantum dot solids. *Nat Mater*. 2016;15:557–563. <https://doi.org/10.1038/nmat4576>
- [10] Pal A, Zhang S, Chavan T, Agashiwala K, Yeh C, Cao W, Banerjee K. Quantum-engineered devices based on 2D materials for next-generation information processing and storage. *Adv Mater*. 2022;35:2109894. <https://doi.org/10.1002/adma.202109894>
- [11] Jing F, Zhang Z, Qin G, Luo G, Cao G, Li H, Song X, Guo G. Gate-controlled quantum dots based on 2D materials. *Adv Quantum Technol*. 2022;5:2100162. <https://doi.org/10.1002/qute.202100162>
- [12] Liu X, Qin X, Li X, Ding Z, Li X, Hu W, Yang J. Designing two-dimensional versatile room-temperature ferromagnets via assembling large-scale magnetic quantum dots. *Nano Lett*. 2021;21:9816–9823. <https://doi.org/10.1021/acs.nanolett.1c03814>
- [13] Matta SK, Tang C, O'Mullane AP, Du A, Russo SP. Density functional theory study of two-dimensional post-transition metal chalcogenides and halides for interfacial charge transport in perovskite solar cells. *ACS Appl Nano Mater*. 2022;5:14456–14463. <https://doi.org/10.1021/acsanm.2c02812>
- [14] Guo B, Liang B, Zheng J, Ahmed S, Krishna S, Ghosh A, Campbell J. Digital alloy-grown InAs/GaAs short-period superlattices with tunable band gaps for short-wavelength infrared photodetection. *ACS Photonics*. 2024;11:1419–1427. <https://doi.org/10.1021/acsphotonics.3c01268>
- [15] Bergeron H, Lebedev D, Hersam MC. Polymorphism in post-dichalcogenide two-dimensional materials. *Chem Rev*. 2021;121:2713–2775. <https://doi.org/10.1021/acs.chemrev.0c00933>
- [16] Giri A, Park G, Jeong U. Layer-structured anisotropic metal chalcogenides: recent advances in synthesis, modulation, and applications. *Chem Rev*. 2023;123:3329–3442. <https://doi.org/10.1021/acs.chemrev.2c00455>
- [17] Li, Xin, et al. "Recent progress on surface chemistry II: Property and characterization." *Chinese Chemical Letters* 36.1 (2025): 110100. <https://doi.org/10.1016/j.ccllet.2024.110100>
- [18] Li, Xin, et al. "Recent progress on surface chemistry I: Assembly and reaction." *Chinese Chemical Letters* 35.12 (2024): 110055. <https://doi.org/10.1016/j.ccllet.2024.110055>
- [19] Wang Y, Yi J. Ferromagnetism in two-dimensional materials via doping and defect engineering. In: Elsevier eBooks. 2020;95–124. <https://doi.org/10.1016/b978-0-08-102154-5.00008-4>
- [20] Lei Z, Sathish CI, Geng X, Guan X, Liu Y, Wang L, Qiao L, Vinu A, Yi J. Manipulation of ferromagnetism in intrinsic two-dimensional magnetic and nonmagnetic materials. *Matter*. 2022;5:4212–4273. <https://doi.org/10.1016/j.matt.2022.11.017>



- [21] Fei Z, Huang B, Malinowski P, Wang W, Song T, Sanchez J, Yao W, Xiao D, Zhu X, May AF, Wu W, Cobden DH, Chu J-H, Xu X. Two-dimensional itinerant ferromagnetism in atomically thin Fe₃GeTe₂. *Nat Mater*. 2018;17:778–782. <https://doi.org/10.1038/s41563-018-0149-7>
- [22] Deng Y, Yu Y, Song Y, Zhang J, Wang NZ, Sun Z, Yi Y, Wu YZ, Wu S, Zhu J, Wang J, Chen XH, Zhang Y. Gate-tunable room-temperature ferromagnetism in two-dimensional Fe₃GeTe₂. *Nature*. 2018;563:94–99. <https://doi.org/10.1038/s41586-018-0626-9>
- [23] You J-Y, Gu B, Maekawa S, Su G. Microscopic mechanism of high-temperature ferromagnetism in Fe, Mn, and Cr-doped InSb, InAs, and GaSb magnetic semiconductors. *Phys Rev B*. 2020;102:094432. <https://doi.org/10.1103/physrevb.102.094432>
- [24] Goel S, Anh LD, Ohya S, Tanaka M. Ferromagnetic resonance and control of magnetic anisotropy by epitaxial strain in the ferromagnetic semiconductor (Ga_{0.8},Fe_{0.2}). *Phys Rev B*. 2019;99:014431. <https://doi.org/10.1103/physrevb.99.014431>
- [25] Takiguchi K, Anh LD, Chiba T, Koyama T, Chiba D, Tanaka M. Giant gate-controlled proximity magnetoresistance in semiconductor-based ferromagnetic–non-magnetic bilayers. *Nat Phys*. 2019;15:1134–1139. <https://doi.org/10.1038/s41567-019-0621-6>
- [26] Schuler B, Lee J-H, Kastl C, Cochrane KA, Chen CT, Refaely-Abramson S, Yuan S, Van Veen E, Roldán R, Borys NJ, Koch RJ, Aloni S, Schwartzberg AM, Ogletree DF, Neaton JB, Weber-Bargioni A. How substitutional point defects in two-dimensional WS₂ induce charge localization, spin–orbit splitting, and strain. *ACS Nano*. 2019;13:10520–10534. <https://doi.org/10.1021/acsnano.9b04611>
- [27] Andrich P, De Las Casas CF, Liu X, Bretscher HL, Berman JR, Heremans FJ, Nealey PF, Awschalom DD. Long-range spin wave mediated control of defect qubits in nanodiamonds. *NPJ Quantum Inf*. 2017;3:29. <https://doi.org/10.1038/s41534-017-0029>
- [28] Ivády V, Abrikosov IA, Gali A. First principles calculation of spin-related quantities for point defect qubit research. *NPJ Comput Mater*. 2018;4:13. <https://doi.org/10.1038/s41524-018-0132-5>
- [29] Pan Y, Yang J, Erwin SC, Kanisawa K, Fölsch S. Reconfigurable quantum-dot molecules created by atom manipulation. *Phys Rev Lett*. 2015;115:076803. <https://doi.org/10.1103/physrevlett.115.076803>
- [30] Zhao G, Ma W, Yu S, Zhang J, Wu K. Orbital mixing between colloidal quantum dots and surface-bound molecules. *J Phys Chem Lett*. 2022;13:11892–11898. <https://doi.org/10.1021/acs.jpcclett.2c03538>
- [31] Leon RCC, Yang CH, Hwang JCC, Lemyre JC, Tantt T, Huang W, Chan KW, Tan KY, Hudson FE, Itoh KM, Morello A, Laucht A, Pioro-Ladrière M, Saraiva A, Dzurak AS. Coherent spin control of s-, p-, d- and f-electrons in a silicon quantum dot. *Nat Commun*. 2020;11:1. <https://doi.org/10.1038/s41467-019-14053-w>
- [32] Kaledin AL, Hill CL, Lian T, Musaev DG. Modulating electronic coupling at the quantum dot/molecule interface by wavefunction engineering. *J Chem Phys*. 2019;150:124112. <https://doi.org/10.1063/1.5083056>



- [33] Fang M, Yang E-H. Advances in two-dimensional magnetic semiconductors via substitutional doping of transition metal dichalcogenides. *Materials*. 2023;16:3701. <https://doi.org/10.3390/ma16103701>
- [34] Hong H, Wu C, Zhao Z, Zuo Y, Wang J, Liu C, Zhang J, Wang F, Feng J, Shen H, Yin J, Wu Y, Zhao Y, Liu K, Gao P, Meng S, Wu S, Sun Z, Liu K, Xiong J. Giant enhancement of optical nonlinearity in two-dimensional materials by multiphoton-excitation resonance energy transfer from quantum dots. *Nat Photonics*. 2021;15:510–515. <https://doi.org/10.1038/s41566-021-00801-2>
- [35] Chowdhury SM, Hossain I, and Chowdhury MR. "Interstitial TM–P pairing in P₃-coordinated wide-gap quantum dots: spin-selective insulating states and enhanced hyperpolarizability." *Nanoscale*, 2026;18:2811–2829. <https://doi.org/10.1039/D5NR02041G>
- [36] Rejali R, Coffey D, Gobeil J, González JW, Delgado F, Otte AF. Complete reversal of the atomic unquenched orbital moment by a single electron. *NPJ Quantum Mater*. 2020;5:1. <https://doi.org/10.1038/s41535-020-00262-w>
- [37] Wieliczka BM, Kaledin AL, Buhro WE, Loomis RA. Wave function engineering in CdSe/PbS core/shell quantum dots. *ACS Nano*. 2018;12:5539–5550. <https://doi.org/10.1021/acsnano.8b01248>
- [38] Xie Z, Zhao T, Yu X, Wang J. Nonlinear optical properties of 2D materials and their applications. *Small*. 2024;20:11621. <https://doi.org/10.1002/sml.202311621>
- [39] Wang X, Zhang A, Qiu S, Zhao L, Chang Y, Liu H, Gao J. Significant enhancement of the second harmonic generation in Janus α -In/GaSe₃ structures. *Phys Rev B*. 2025;111:155412. <https://doi.org/10.1103/physrevb.111.155412>
- [40] Wang Q, Zhang H-L. *Two-Dimensional Materials for Nonlinear Optics: Fundamentals, Preparation Methods, and Applications*. John Wiley & Sons; 2023. <https://doi.org/10.1002/9783527838288>
- [41] Taghizadeh A, Thygesen KS, Pedersen TG. Two-dimensional materials with giant optical nonlinearities near the theoretical upper limit. *ACS Nano*. 2021;15:7155–7167. <https://doi.org/10.1021/acsnano.1c00344>
- [42] Boyd RW. *Nonlinear Optics*, 4th ed.; Academic Press: London, 2020. <https://doi.org/10.1016/c2015-0-05510-1>
- [43] Alam MZ, De Leon I, Boyd RW. Large optical nonlinearity of indium tin oxide in its epsilon-near-zero region. *Science*. 2016;352:795–797. <https://doi.org/10.1126/science.aae0330>
- [44] Frisch MJ, Trucks GW, Schlegel HB, Scuseria GE, Robb MA, Cheeseman JR, Scalmani G, Barone V, Petersson GA, Nakatsuji H, Li X, Caricato M, Marenich A, Bloino J, Janesko BG, Gomperts R, Mennucci B, Hratchian HP, Ortiz JV, Izmaylov AF, Sonnenberg JL, Williams-Young D, Ding F, Lipparini F, Egidi F, Goings J, Peng B, Petrone A, Henderson T, Ranasinghe D, Zakrzewski VG, Gao J, Rega N, Zheng G, Liang W, Hada M, Ehara M, Toyota K, Fukuda R, Hasegawa J, Ishida M, Nakajima T, Honda Y, Kitao O, Nakai H, Vreven T, Throssell K, Montgomery JA Jr, Peralta JE, Ogliaro F, Bearpark M, Heyd JJ, Brothers E, Kudin KN, Staroverov VN, Keith T, Kobayashi R, Normand J, Raghavachari K, Rendell A, Burant JC, Iyengar SS, Tomasi J, Cossi M, Millam JM, Klene M, Adamo C, Cammi R, Ochterski JW, Martin RL, Morokuma K, Farkas O, Foresman JB, Fox DJ. *Gaussian 09*, Revision A.02; Gaussian, Inc.: Wallingford CT, 2016



- [45] Chai, J.-D.; Head-Gordon, M. Long-range corrected hybrid density functionals with damped atom–atom dispersion corrections. *Physical Chemistry Chemical Physics* 2008, 10 (44), 6615. <https://doi.org/10.1039/b810189b>.
- [46] Hay, P. J.; Wadt, W. R. Ab Initio Effective Core Potentials for Molecular Calculations. Potentials for the Transition Metal Atoms Sc to Hg. *J. Chem. Phys.* 1985, 82 (1), 270–283. <https://doi.org/10.1063/1.448799>.
- [47] Qu Z, Liu C. Intrinsic magnetism in edge-reconstructed zigzag graphene nanoribbons. In: Raza H, ed. *Graphene Nanoelectronics: Metrology, Synthesis, Properties and Applications*. Wiley-VCH; 2013. p. 9–28. <https://doi.org/10.1002/9781118691281.ch2>
- [48] Kalamse V, Gaikwad S, Chaudhari A. Computational study of 5d transition metal mononitrides and monoborides using density functional method. *Bull Mater Sci.* 2010;33:233–238. <https://doi.org/10.1007/s12034-010-0036-6>
- [49] Beck, Philip. Tuning the Spin-Orbit Coupling and the Spin Dynamics of Atomic Chains on Superconductors. Diss. Staats-und Universitätsbibliothek Hamburg Carl von Ossietzky, 2022. <https://ediss.sub.uni-hamburg.de/handle/ediss/9900>
- [50] Majumdar, Sayani, P. Avramov, and S. Sakai. "Manipulating spins at molecular level: an insight into the ferromagnet-organic interface." *World Sci. Reference Spin Organics 2* (2018): 1-61.
- [51] Wang, Binbin. Advanced Magnetic Characterization using Electron Microscopy and its Application on Spintronic Devices. The Ohio State University, 2022. <https://www.proquest.com/openview/00ec58e48dff1789bef2f890a1f55d56/1?pq-origsite=gscholar&cbl=18750&diss=y>
- [52] Streubel, Robert, et al. "Magnetism in curved geometries." *Journal of Physics D: Applied Physics* 49.36 (2016): 363001. <https://doi.org/10.1088/0022-3727/49/36/363001>



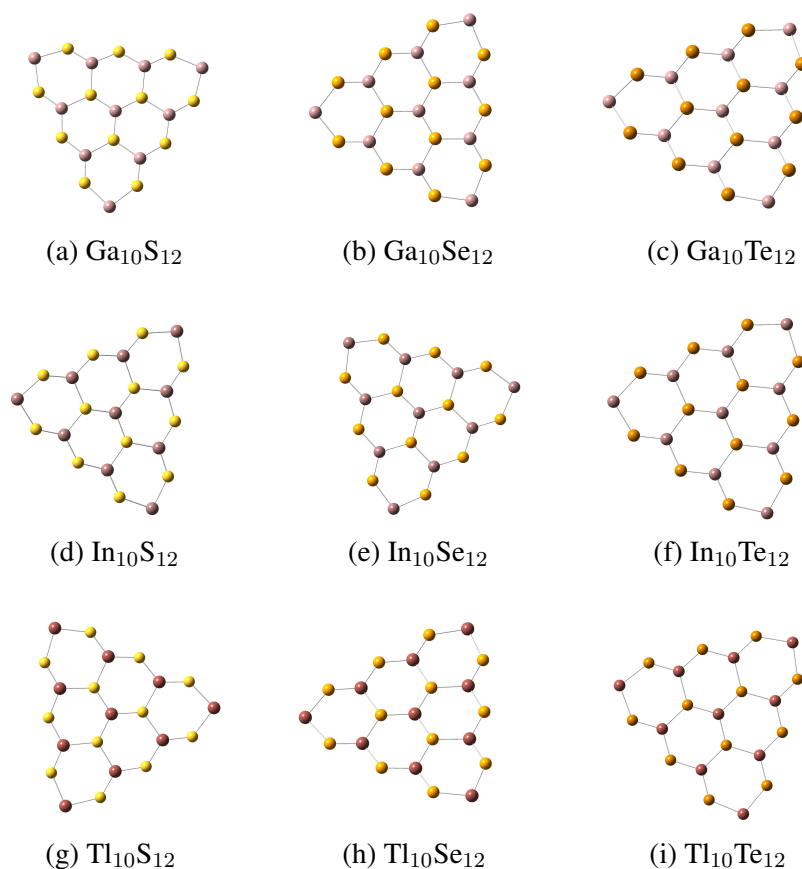


Figure 1: Single-atom-thick, triangular $\text{M}_{10}\text{X}_{12}$ quantum dots with zigzag edges, structurally derived from honeycomb-shaped 2D metal-chalcogenide nanoflakes. Each bond lengths are ranges approximately from 2.1 Å to 3.2 Å. The edge-effects and geometric confinement induces critical influence on their electronic structure and emergence of distinctive properties.



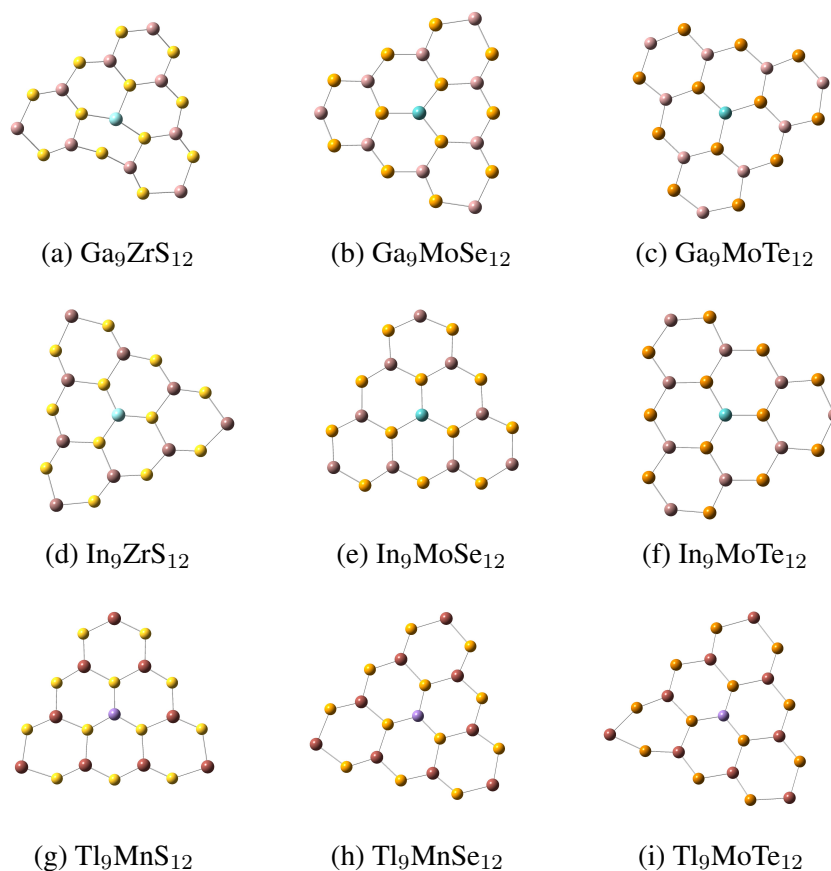
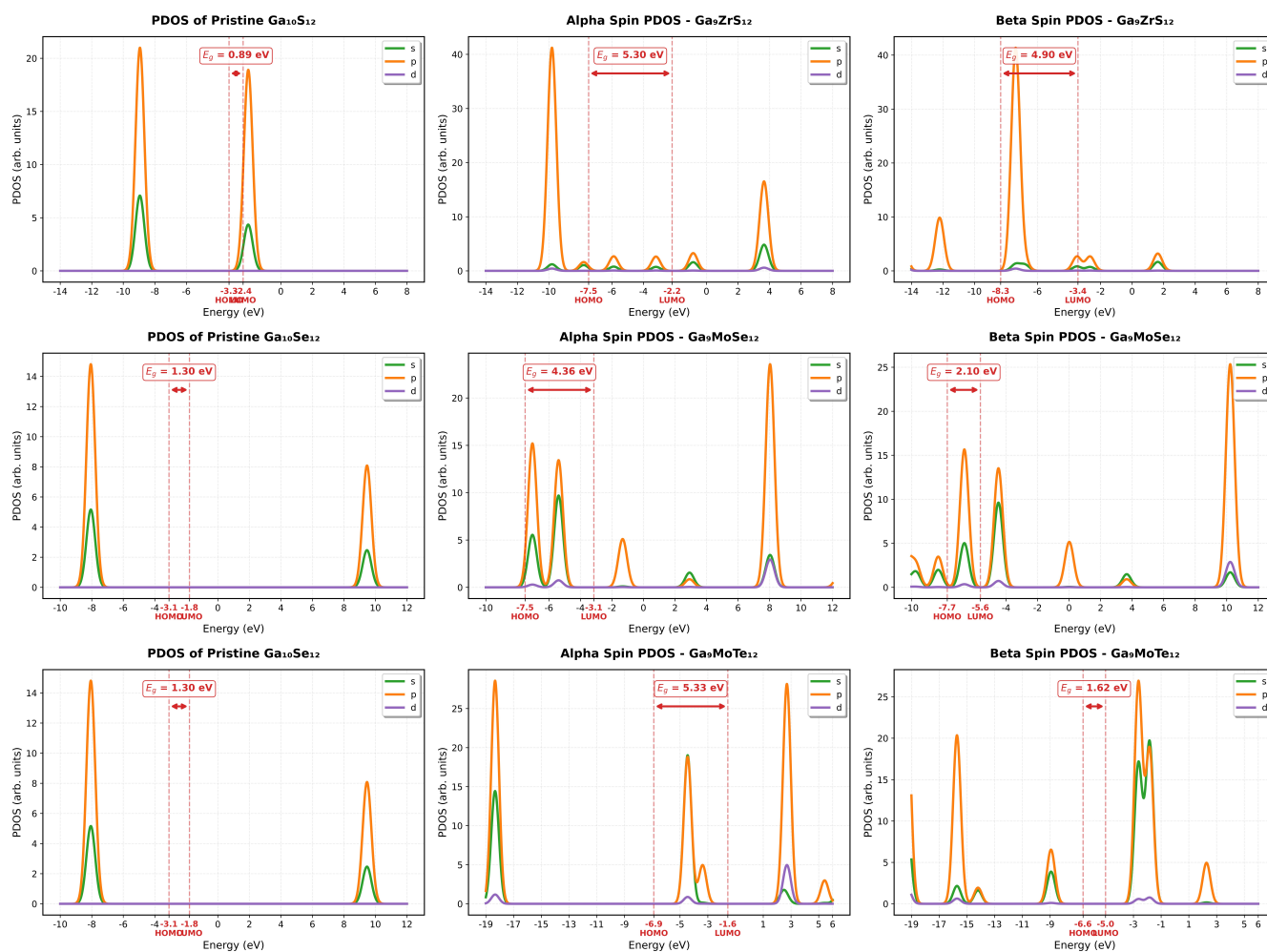


Figure 2: TM-substituted counterparts of the pristine nanodots with chalcogen-coordinated point defects (X_3 sites). Such localized defects disrupt the inversion symmetry of the configurations and demonstrate highly controllable multifunctional responses in real-space.

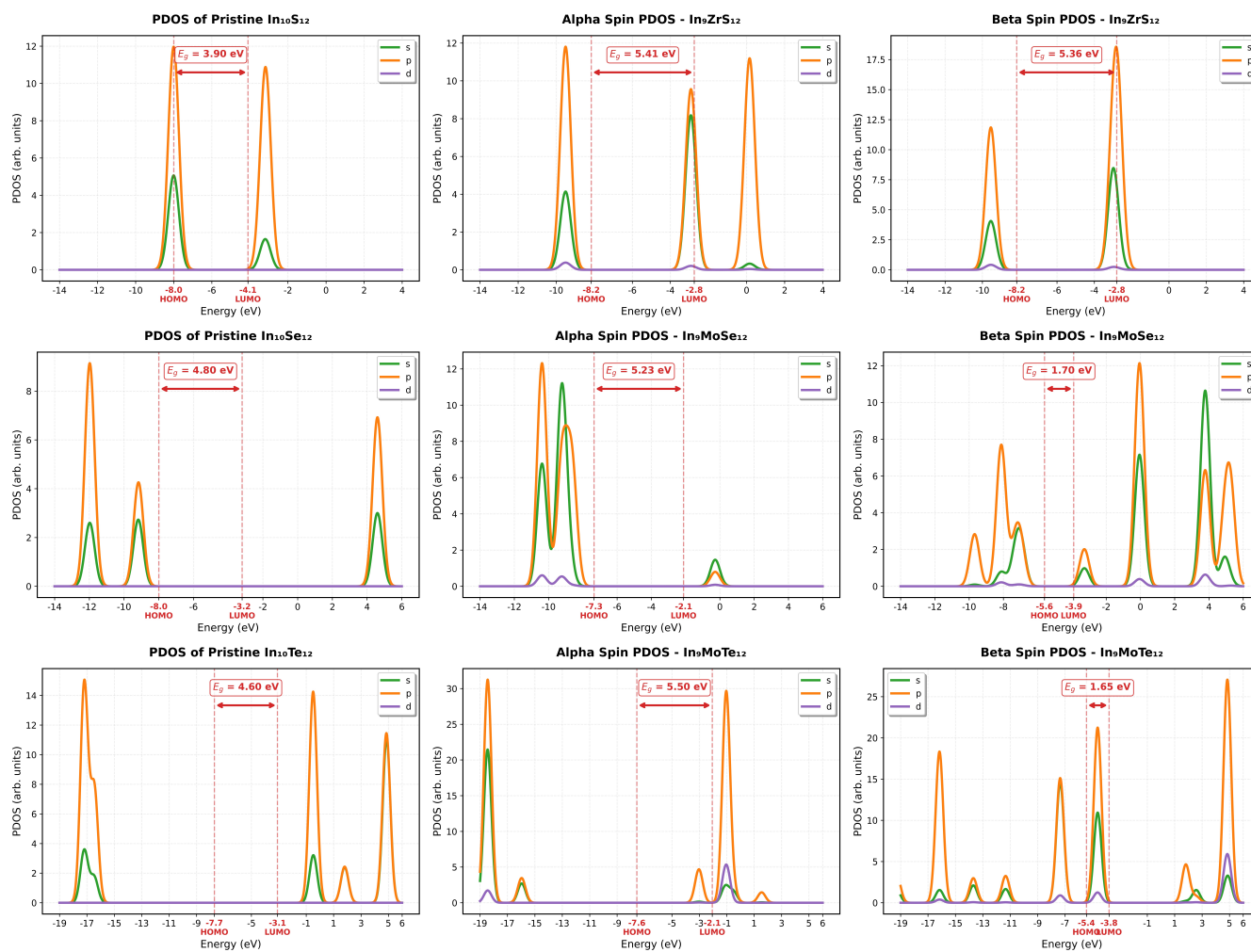




(a)

Figure 3(a): Partial Density of States plotted for different orbitals in Ga-based systems. The data correspond to pristine $\text{Ga}_{10}\text{X}_{12}$, Zr-doped Ga_9S_{12} , and Mo-doped $\text{Ga}_9(\text{Se},\text{Te})_{12}$ configurations, with internal titles indicating the specific composition in each case.

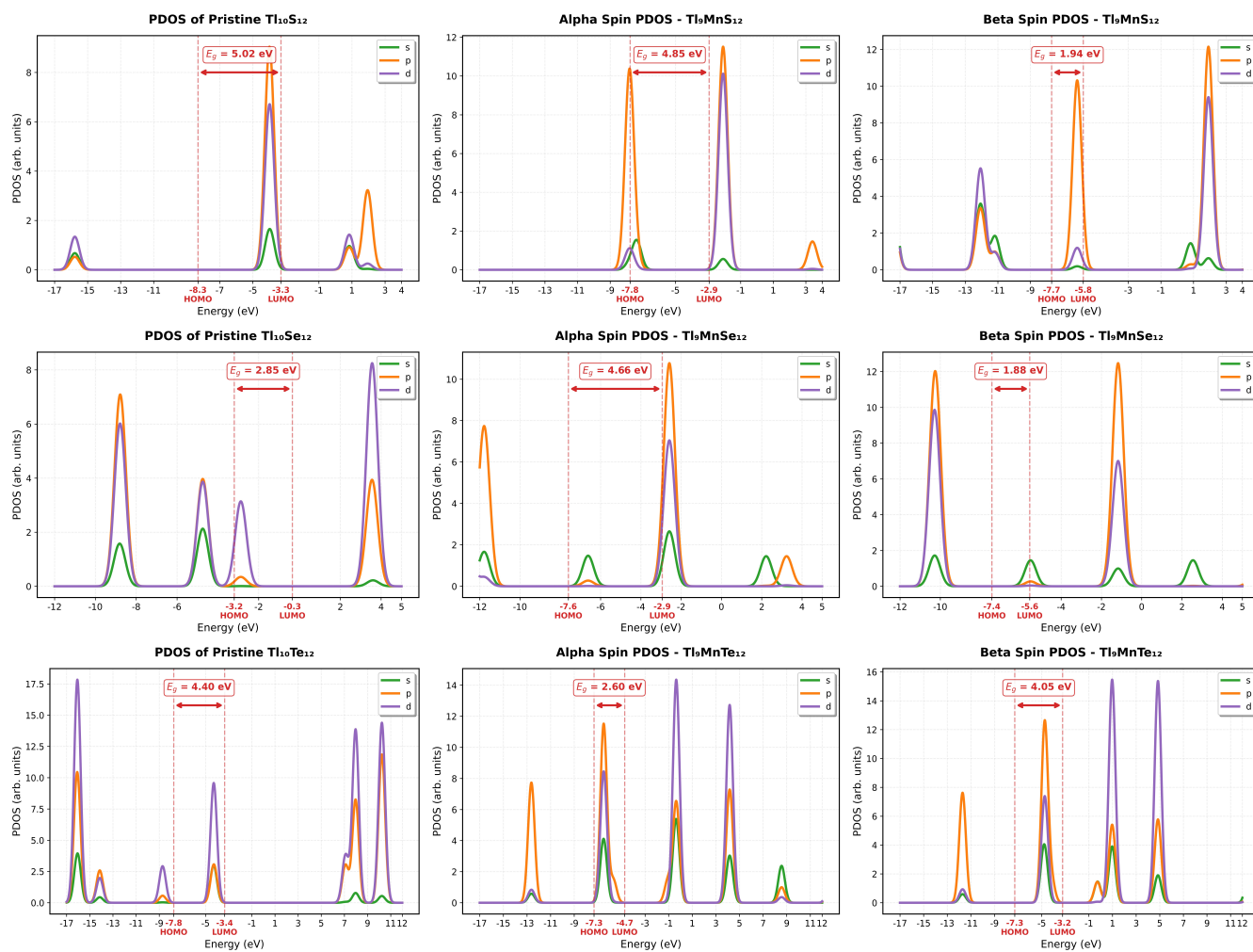




(b)

Figure 3(b): Partial Density of States plotted for different orbitals in In-based systems. The data correspond to pristine $\text{In}_{10}\text{X}_{12}$, Zr-doped In_9S_{12} , and Mo-doped $\text{In}_9(\text{Se},\text{Te})_{12}$ configurations, with internal titles indicating the specific composition in each case.





(c)

Figure 3(c): Partial Density of States plotted for different orbitals in Tl-based systems. The data correspond to pristine $\text{Tl}_{10}\text{X}_{12}$, and Mn-doped $\text{Tl}_9(\text{S}, \text{Se}, \text{Te})_{12}$ configurations, with internal titles indicating the specific composition in each case.



Figure 3(a–c): Orbital-projected PDOS plotted for the pristine and the doped configurations comprises each of the orbital's total contribution. All of the plots showing a well-defined HOMO-LUMO gap with distinct lower energy and higher energy spectrum in the potential landscape. For the pristine QDs, the largest HOMO-LUMO gap was derived for $\text{Tl}_{10}\text{S}_{12}$ (5.02 eV), and the lowest was found for $\text{Ga}_{10}\text{S}_{12}$ (0.89 eV). After the central perturbation with TM, emergence of new hybridized electronic states around and near the energy gap is observed. These localized states are spin-dependent by nature, as we can see the overlapping states energetically varies between the alpha- and beta-spin orbitals. Such variation is very high when TM's *d*-orbital has higher unpaired electrons, and this controllable feature not only allows modification of pristine's orbital redistributions and fine texture of spin densities, but also enhances the nonlinear responses and the intrinsic spin-orbit coupling, respectively. The largest energy gap was exhibited by the $\alpha\text{-In}_9\text{ZrS}_{12}$ (5.41 eV) while the smallest was captured for the $\beta\text{-Ga}_9\text{MoTe}_{12}$ (1.62 eV). All PDOS are aligned to a common reference energy (set at 0 eV) for each system to allow direct comparison.



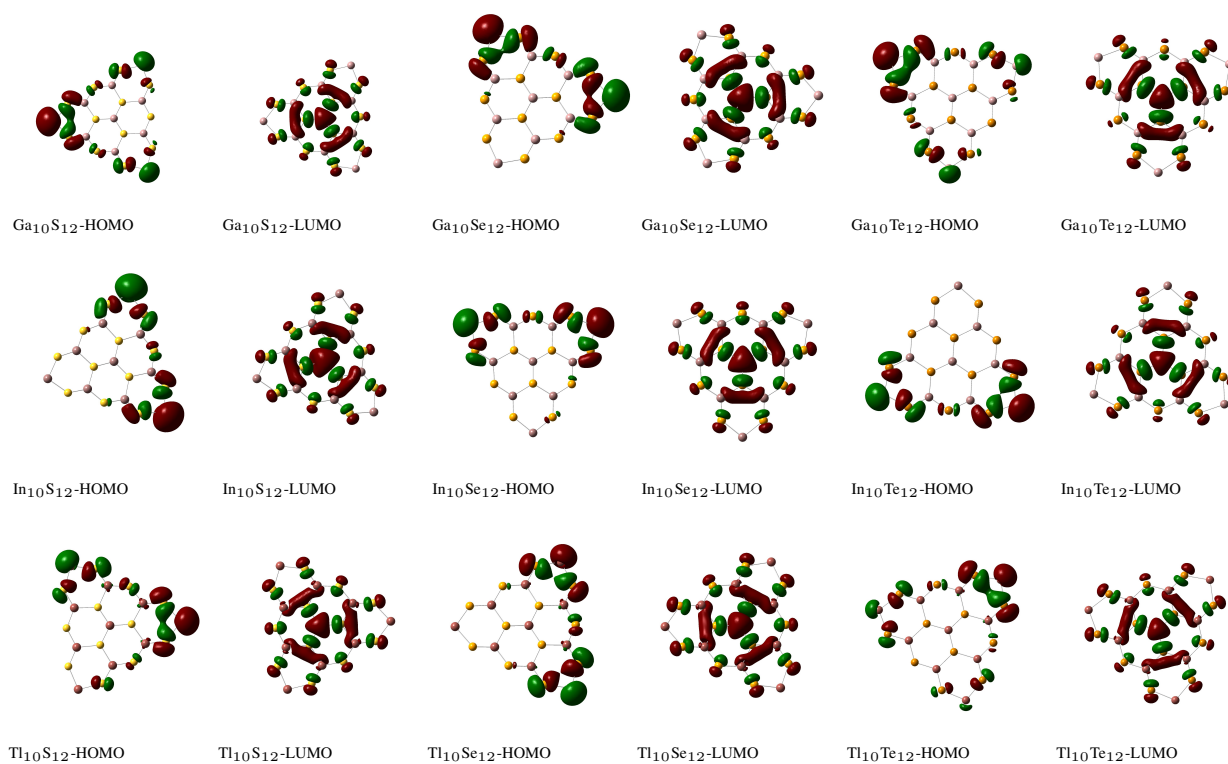


Figure 4: Isosurface plots of the frontier molecular orbitals for pristine configurations. Red and green regions represent the phase of the orbital wavefunctions, showing where electron density is distributed between atoms. This distribution tells us at which location in the real space, bonding interactions of electrons occupy (the most probable) a molecular region when just below (HOMO) or above (LUMO) the energy gap center. Such asymmetric lateral distribution of MO explains the intrinsic electronic structure of the nonmagnetic host and provides a baseline to understand how doping-induced perturbations would modulate orbital character in a site-specific manner.



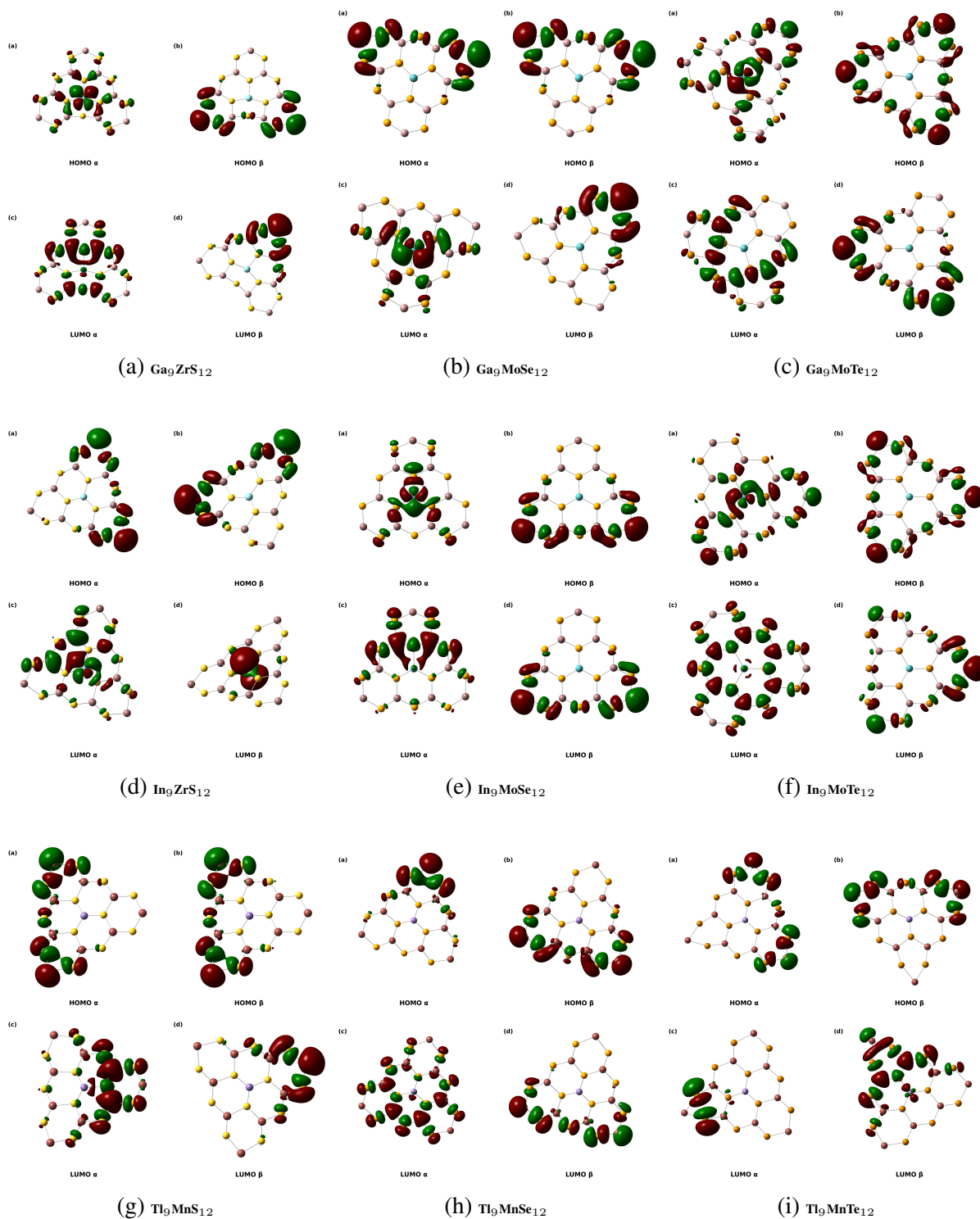


Figure 5(a–i): Isosurface plots of the frontier molecular orbitals for TM-doped configurations. Orbital relocation and distinct spin-selective distribution are observed due to the formation of local TM-X₃ point defects. The wavefunctions show spin-dependent localization, either concentrate around the defect center or redistribute toward edge sites, and remain spatially orthogonal for same-spin orbitals of different energies. Among the configurations, β of Zr-(S)₃, and Mn-(S/Te)₃ coordination exhibits comparatively more pronounced spatial modulation, charge concentration, and orbitals reorganization in the host quantum dots.



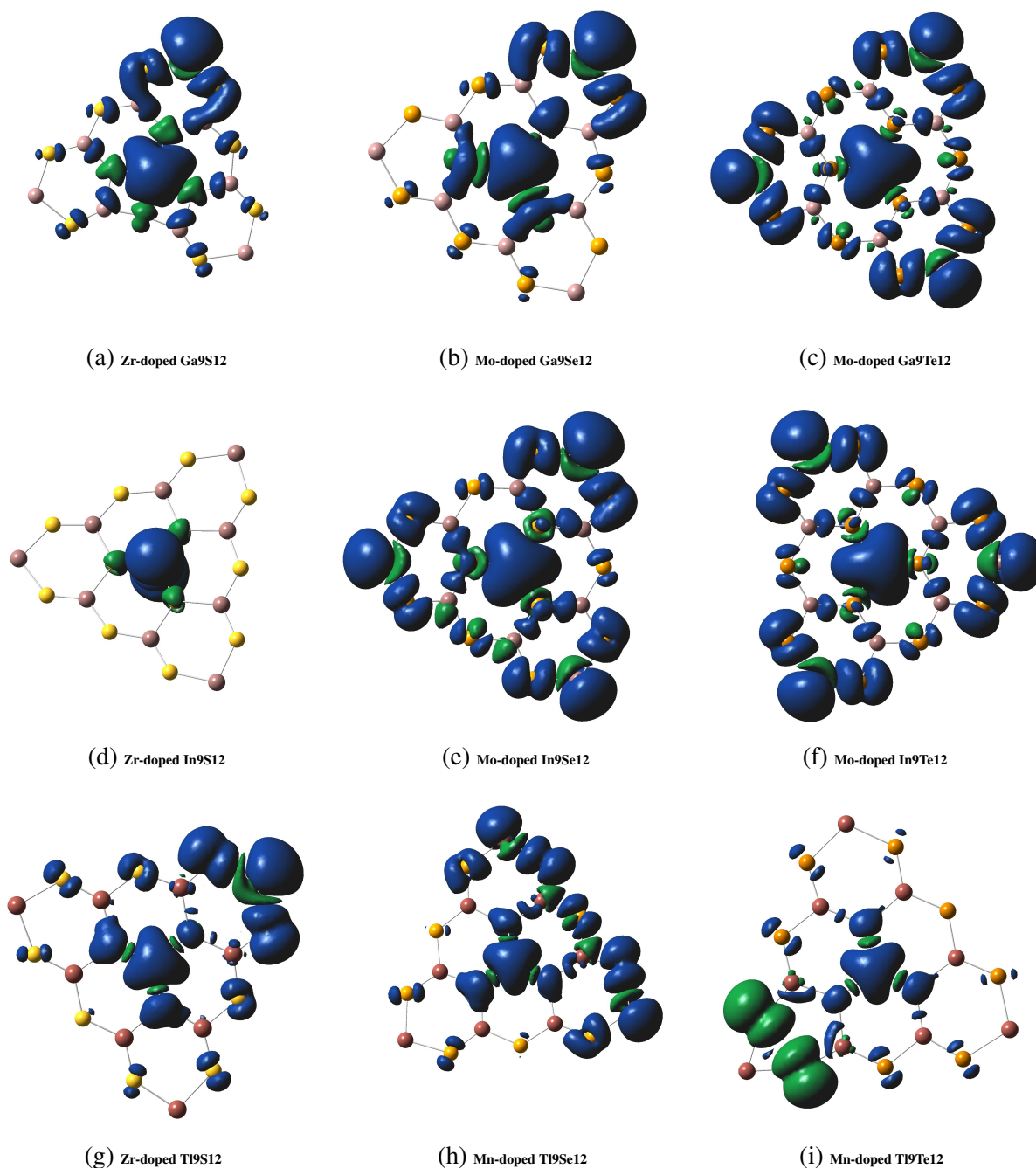


Figure 6: Spin density distribution of spin-up (green) and spin-down (blue) orbitals in the defected nanodots. The dominant spin-down components show preferential spin-polarization with distinct spatial localization around the central defect or redistribution toward specific edge sites, depending on the host configuration. This answers how selective hybridizations tends to favor specific spin-channels that can have access to more electronic states (hence resulting in a lower energy gap in the corresponding orbitals) within a confined geometry.



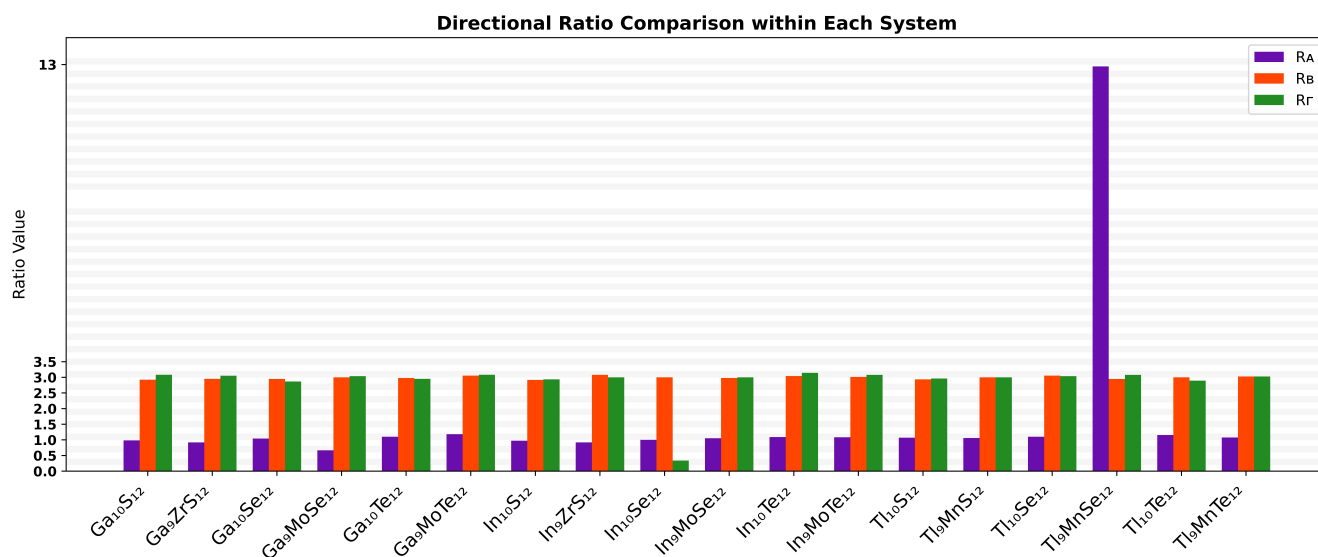


Figure 7: Directional sensitivity (R_A , R_B , R_Γ) derived from linear polarizability, first- and second-hyperpolarizability, respectively. This comparison basically describes the degree of directional uniformity retained in the substituted systems, even though they exhibit colossal nonlinear intensities along different components. The R_A ranges from 0.97 to 1.15 for pristine systems and from 0.67 to 12.94 for centrally perturbed systems, which indicates the anisotropic response of linear polarizability remains relatively uniform in most cases, but shows significant variation in Mn-doped Tl₉Se₁₂. In contrast, the static hyperpolarizabilities exhibit much more consistency in directional behavior, with all the configurations has R_B values ranging from 2.9 to ~ 3 , and R_Γ from 2.9 to 3.1, respectively. The only exception is In₁₀Se₁₂ QD, which has a ratio of 0.34, indicates its orthogonal direction is more responsive to the external field. Such preserved directional sensitivity with a high increment in nonlinear response suggests substantial anisotropic behavior of these nanoflakes under an external electric field.



Table 1: Structural parameters of pristine and TM-substituted PTMC QDs. D_{\max} : maximum diameter; R_g : radius of gyration; \bar{d} : average bond length; $d_{\text{TM-X}}$: dopant–neighbor bond lengths.

System	Pristine QD				Doped QD				
	D_{\max} (Å)	R_g (Å)	\bar{d} (Å)	d_{\min} – d_{\max} (Å)	D_{\max} (Å)	R_g (Å)	\bar{d} (Å)	d_{\min} – d_{\max} (Å)	$d_{\text{TM-X}}$ (Å)
<i>Ga-based QDs</i>									
Ga ₁₀ S ₁₂ / Ga ₉ ZrS ₁₂	12.733	5.021	2.345	2.130–2.625	13.110	5.034	2.366	2.130–2.764	2.558, 2.523, 2.558
Ga ₁₀ Se ₁₂ / Ga ₉ MoSe ₁₂	13.217	5.270	2.470	2.259–2.753	13.260	5.267	2.466	2.264–2.786	2.527, 2.517, 2.527
Ga ₁₀ Te ₁₂ / Ga ₉ MoTe ₁₂	14.075	5.656	2.659	2.455–2.954	13.713	5.605	2.624	2.538–2.750	2.750, 2.750, 2.750
<i>In-based QDs</i>									
In ₁₀ S ₁₂ / In ₉ ZrS ₁₂	13.631	5.369	2.495	2.293–2.740	13.662	5.397	2.504	2.294–2.750	2.432, 2.432, 2.432
In ₁₀ Se ₁₂ / In ₉ MoSe ₁₂	14.128	5.627	2.628	2.421–2.890	13.740	5.526	2.585	2.483–2.733	2.663, 2.637, 2.636
In ₁₀ Te ₁₂ / In ₉ MoTe ₁₂	14.990	6.017	2.822	2.609–3.113	14.451	5.895	2.768	2.691–2.874	2.788, 2.788, 2.788
<i>Tl-based QDs</i>									
Tl ₁₀ S ₁₂ / Tl ₉ MnS ₁₂	14.292	5.646	2.625	2.406–2.891	14.298	5.517	2.587	2.391–2.920	2.391, 2.449, 2.391
Tl ₁₀ Se ₁₂ / Tl ₉ MnSe ₁₂	14.748	5.888	2.748	2.530–3.022	14.585	5.756	2.709	2.495–3.029	2.525, 2.495, 2.525
Tl ₁₀ Te ₁₂ / Tl ₉ MnTe ₁₂	15.586	6.269	2.937	2.715–3.236	15.950	6.174	2.912	2.670–3.269	2.671, 2.693, 2.670



Table 2: Electronic and magnetic properties of group-13-based MX configurations. (a) pristine structures, (b) TM-substituted reconstructed structures, (c) magnetic responses due to interaction with external field.

(a)

Host	E_b (eV)	E_g (eV)	μ_0 (a.u.)
Ga ₁₀ S ₁₂	3.64	0.89	0.0022
Ga ₁₀ Se ₁₂	3.32	1.30	0.0026
Ga ₁₀ Te ₁₂	2.83	3.50	0.0203
In ₁₀ S ₁₂	3.47	3.90	0.0029
In ₁₀ Se ₁₂	3.17	4.80	0.0013
In ₁₀ Te ₁₂	2.72	4.60	0.0015
Tl ₁₀ S ₁₂	3.15	5.02	0.0242
Tl ₁₀ Se ₁₂	2.92	2.85	0.0169
Tl ₁₀ Te ₁₂	2.53	4.40	0.0261

(b)

Host	Dp	E_{form} (eV)	E_b (eV)	E_g^{\uparrow} (eV)	E_g^{\downarrow} (eV)	μ_0 (a.u.)
Ga ₉ S ₁₂	Zr	-4.78	3.86	5.30	4.90	1.8587
Ga ₉ Se ₁₂	Mo	-4.90	3.55	4.36	2.10	4.2452
Ga ₉ Te ₁₂	Mo	-4.54	3.10	5.33	1.62	5.9322
In ₉ S ₁₂	Zr	-5.17	3.70	5.41	5.36	0.0033
In ₉ Se ₁₂	Mo	-4.74	3.40	5.23	1.70	6.8281
In ₉ Te ₁₂	Mo	-4.88	2.94	5.50	1.65	0.0079
Tl ₉ S ₁₂	Mn	-4.84	3.40	4.85	1.94	3.0787
Tl ₉ Se ₁₂	Mn	-4.20	3.10	4.66	1.88	1.9514
Tl ₉ Te ₁₂	Mn	-4.62	2.73	2.60	4.05	5.3514

(c)

Host	Dp	M	μ_{net} (μ_B)	Δg_{xx}	Δg_{yy}	Δg_{zz}	g_{eff}	μ_{eff} (μ_B)
Ga ₉ S ₁₂	Zr	4	3.00	-1.076	-0.998	-0.146	1.26	2.44
Ga ₉ Se ₁₂	Mo	6	5.00	-0.434	-0.275	-0.010	1.76	5.22
Ga ₉ Te ₁₂	Mo	8	7.00	0.494	1.141	5.862	4.50	17.86
In ₉ S ₁₂	Zr	2	1.00	-0.204	-0.204	-0.003	1.87	1.62
In ₉ Se ₁₂	Mo	8	7.00	0.048	0.424	0.650	2.38	9.43
In ₉ Te ₁₂	Mo	8	7.00	0.884	0.892	8.042	5.28	20.93
Tl ₉ S ₁₂	Mn	7	6.00	0.032	0.149	0.231	2.14	7.41
Tl ₉ Se ₁₂	Mn	7	6.00	0.947	1.632	2.481	3.70	12.78
Tl ₉ Te ₁₂	Mn	5	4.00	-1.232	-1.207	-0.073	1.17	2.85



Table 3: Spatial density-density correlation between same-spin orbitals of different energies.

System	Channel	Overlap pair	D_{HL}	\tilde{D}_{HL}
Ga ₉ ZrS ₁₂	α	H α -L α	3.3888×10^{-4}	0.0746
	β	H β -L β	3.1734×10^{-5}	0.0103
Ga ₉ MoSe ₁₂	α	H α -L α	5.1302×10^{-5}	0.0104
	β	H β -L β	3.2719×10^{-5}	0.0123
Ga ₉ MoTe ₁₂	α	H α -L α	1.5198×10^{-4}	0.0594
	β	H β -L β	8.9530×10^{-4}	0.7851
In ₉ ZrS ₁₂	α	H α -L α	1.0305×10^{-4}	0.0350
	β	H β -L β	1.5528×10^{-5}	0.0043
In ₉ MoSe ₁₂	α	H α -L α	2.4522×10^{-4}	0.0536
	β	H β -L β	1.4173×10^{-3}	0.9492
In ₉ MoTe ₁₂	α	H α -L α	2.2926×10^{-4}	0.1213
	β	H β -L β	7.4158×10^{-4}	0.7850
Tl ₉ MnS ₁₂	α	H α -L α	1.0665×10^{-4}	0.0489
	β	H β -L β	3.1691×10^{-5}	0.0109
Tl ₉ MnSe ₁₂	α	H α -L α	1.6890×10^{-4}	0.0928
	β	H β -L β	1.7834×10^{-3}	0.8797
Tl ₉ MnTe ₁₂	α	H α -L α	1.8716×10^{-5}	0.0081
	β	H β -L β	6.1843×10^{-5}	0.0477



Table 4: HOMO–LUMO overlap integrals from signed real-space wavefunction, normalized overlaps, and electronic spatial extents ($\langle r^2 \rangle$ in Bohr²) for all structures and spin channels.

System	Channel	Overlap pair	S	$ S_{\text{norm}} $	$\langle r^2 \rangle_H$	$\langle r^2 \rangle_L$
Ga ₉ ZrS ₁₂	α	H α –L α	1.2474×10^{-6}	0.0000	26.5133	73.4516
	β	H β –L β	1.7430×10^{-6}	0.0000	182.1451	165.0047
Ga ₉ MoSe ₁₂	α	H α –L α	-3.8323×10^{-5}	0.0000	188.4636	30.0014
	β	H β –L β	-1.9331×10^{-6}	0.0000	188.3397	184.7601
Ga ₉ MoTe ₁₂	α	H α –L α	-1.2736×10^{-6}	0.0000	80.1892	99.1496
	β	H β –L β	-9.4803×10^{-6}	0.0000	189.8775	202.7604
In ₉ ZrS ₁₂	α	H α –L α	2.6031×10^{-5}	0.0000	215.4526	57.3589
	β	H β –L β	-8.6911×10^{-6}	0.0000	215.4633	18.0892
In ₉ MoSe ₁₂	α	H α –L α	-1.3074×10^{-4}	0.0001	33.8344	94.8511
	β	H β –L β	2.2814×10^{-4}	0.0002	203.5608	214.1154
In ₉ MoTe ₁₂	α	H α –L α	-7.8615×10^{-5}	0.0001	99.3915	114.9374
	β	H β –L β	-6.7803×10^{-4}	0.0007	214.9433	228.5232
Tl ₉ MnS ₁₂	α	H α –L α	6.4360×10^{-6}	0.0000	192.6453	99.3229
	β	H β –L β	1.1188×10^{-6}	0.0000	193.1523	191.1198
Tl ₉ MnSe ₁₂	α	H α –L α	1.7724×10^{-4}	0.0002	206.9119	111.9279
	β	H β –L β	-1.4000×10^{-5}	0.0000	200.9388	198.8377
Tl ₉ MnTe ₁₂	α	H α –L α	3.4190×10^{-5}	0.0000	228.2090	182.6864
	β	H β –L β	6.4570×10^{-7}	0.0000	228.2522	146.3248



Table 5: Calculated static linear polarizability and higher-order hyperpolarizabilities (α , β , γ) for the considered quantum dots.

Host	Dp	α_{iso} (a.u.)	α_{aniso} (a.u.)	β_{\parallel} (a.u.)	β_{\perp} (a.u.)	γ_{\parallel} (a.u.)	γ_{\perp} (a.u.)
Ga ₁₀ S ₁₂	–	6.1×10^2	6.0×10^2	-3.8×10^1	-1.3×10^1	3.7×10^5	1.2×10^5
Ga ₉ S ₁₂	Zr	6.1×10^2	5.6×10^2	1.8×10^3	6.1×10^2	6.1×10^5	2.0×10^5
Ga ₁₀ Se ₁₂	–	7.4×10^2	7.7×10^2	5.6	1.9	4.3×10^5	1.5×10^5
Ga ₉ Se ₁₂	Mo	7.5×10^2	5.0×10^2	4.5×10^3	1.5×10^3	8.2×10^5	2.7×10^5
Ga ₁₀ Te ₁₂	–	1.0×10^3	1.1×10^3	2.8	9.4×10^{-1}	6.2×10^5	2.1×10^5
Ga ₉ Te ₁₂	Mo	1.1×10^3	1.3×10^3	2.2×10^5	7.2×10^4	3.7×10^8	1.2×10^8
In ₁₀ S ₁₂	–	7.3×10^2	7.1×10^2	3.5×10^1	1.2×10^1	9.1×10^5	3.1×10^5
In ₉ S ₁₂	Zr	7.5×10^2	6.9×10^2	2.0×10^1	6.5	9.3×10^5	3.1×10^5
In ₁₀ Se ₁₂	–	8.8×10^2	8.8×10^2	-1.5×10^1	-5.0	2.7×10^5	8.0×10^5
In ₉ Se ₁₂	Mo	9.2×10^2	9.7×10^2	1.4×10^5	4.7×10^4	9.9×10^7	3.3×10^7
In ₁₀ Te ₁₂	–	1.1×10^3	1.2×10^3	-7.6×10^1	-2.5×10^1	1.1×10^6	3.5×10^5
In ₉ Te ₁₂	Mo	1.2×10^3	1.3×10^3	2.2×10^5	7.3×10^4	1.6×10^8	5.2×10^7
Tl ₁₀ S ₁₂	–	8.4×10^2	9.0×10^2	2.7×10^1	9.2	8.0×10^5	2.7×10^5
Tl ₉ S ₁₂	Mn	8.2×10^2	8.7×10^2	3.0×10^3	1.0×10^3	9.9×10^5	3.3×10^5
Tl ₁₀ Se ₁₂	–	1.0×10^3	1.1×10^3	2.2×10^1	7.2	8.2×10^5	2.7×10^5
Tl ₉ Se ₁₂	Mn	1.7×10^2	2.2×10^3	-5.6×10^4	-1.9×10^4	-1.2×10^8	-3.9×10^7
Tl ₁₀ Te ₁₂	–	1.3×10^3	1.5×10^3	1.2×10^2	4.0×10^1	1.1×10^6	3.8×10^5
Tl ₉ Te ₁₂	Mn	1.3×10^3	1.4×10^3	2.3×10^3	7.6×10^2	2.3×10^5	7.6×10^4



Data Availability

Information on supporting data from this study remains privately accessible to the authors who can provide it to qualified requesters upon request.

